



HAL
open science

The structure of steady shock waves in porous metals

Christophe Czarnota, Alain Molinari, Sébastien Mercier

► **To cite this version:**

Christophe Czarnota, Alain Molinari, Sébastien Mercier. The structure of steady shock waves in porous metals. *Journal of the Mechanics and Physics of Solids*, 2017, 107, pp.204-228. 10.1016/j.jmps.2017.06.005 . hal-03279917

HAL Id: hal-03279917

<https://hal.univ-lorraine.fr/hal-03279917>

Submitted on 23 Mar 2022

HAL is a multi-disciplinary open access archive for the deposit and dissemination of scientific research documents, whether they are published or not. The documents may come from teaching and research institutions in France or abroad, or from public or private research centers.

L'archive ouverte pluridisciplinaire **HAL**, est destinée au dépôt et à la diffusion de documents scientifiques de niveau recherche, publiés ou non, émanant des établissements d'enseignement et de recherche français ou étrangers, des laboratoires publics ou privés.



HAL
open science

The structure of steady shock waves in porous metals

Christophe Czarnota, Alain Molinari, Sébastien Mercier

► **To cite this version:**

Christophe Czarnota, Alain Molinari, Sébastien Mercier. The structure of steady shock waves in porous metals. *Journal of the Mechanics and Physics of Solids*, Elsevier, 2017, 107, pp.204-228. 10.1016/j.jmps.2017.06.005 . hal-03279917

HAL Id: hal-03279917

<https://hal.univ-lorraine.fr/hal-03279917>

Submitted on 23 Mar 2022

HAL is a multi-disciplinary open access archive for the deposit and dissemination of scientific research documents, whether they are published or not. The documents may come from teaching and research institutions in France or abroad, or from public or private research centers.

L'archive ouverte pluridisciplinaire **HAL**, est destinée au dépôt et à la diffusion de documents scientifiques de niveau recherche, publiés ou non, émanant des établissements d'enseignement et de recherche français ou étrangers, des laboratoires publics ou privés.

Accepted Manuscript

The structure of steady shock waves in porous metals

Christophe Czarnota, Alain Molinari, Sébastien Mercier

PII: S0022-5096(16)30736-0
DOI: [10.1016/j.jmps.2017.06.005](https://doi.org/10.1016/j.jmps.2017.06.005)
Reference: MPS 3131

To appear in: *Journal of the Mechanics and Physics of Solids*

Received date: 4 November 2016
Revised date: 15 May 2017
Accepted date: 6 June 2017

Please cite this article as: Christophe Czarnota, Alain Molinari, Sébastien Mercier, The structure of steady shock waves in porous metals, *Journal of the Mechanics and Physics of Solids* (2017), doi: [10.1016/j.jmps.2017.06.005](https://doi.org/10.1016/j.jmps.2017.06.005)



This is a PDF file of an unedited manuscript that has been accepted for publication. As a service to our customers we are providing this early version of the manuscript. The manuscript will undergo copyediting, typesetting, and review of the resulting proof before it is published in its final form. Please note that during the production process errors may be discovered which could affect the content, and all legal disclaimers that apply to the journal pertain.

The structure of steady shock waves in porous metals

Christophe Czarnota^{a,*}, Alain Molinari^a, Sébastien Mercier^a

^aLaboratoire d'Etude des Microstructures et de Mécanique des Matériaux, LEM3 - UMR CNRS 7239,
Université de Lorraine - Ile du Saulcy - 57045 METZ Cedex 1 - FRANCE

Abstract

The paper aims at developing an understanding of steady shock wave propagation in a ductile metallic material containing voids. Porosity is assumed to be **less than 0.3** and voids are not connected (foams are not considered). As the shock wave is traveling in the porous medium, the voids are facing a rapid collapse. During this dynamic compaction process, material particles are subjected to very high acceleration in the vicinity of voids, thus generating acceleration forces at the microscale that influence the overall response of the porous material. Analyzing how stationary shocks are influenced by these micro-inertia effects is the main goal of this work. **The focus is essentially on the shock structure, ignoring oscillatory motion of pores prevailing at the tail of the shock wave.** Following the constitutive framework developed by Molinari & Ravichandran [J. Appl. Phys. **95**, 4 (2004)] for the analysis of steady shock waves in dense metals, an analytical approach of steady state propagation of plastic shocks in porous metals is proposed. The initial void size appears as a characteristic internal length that scales the overall dynamic response, thereby contributing to the structuring of the shock front. This key feature is not captured by standard damage models where the porosity stands for the single damage parameter with no contribution of the void size. The results obtained in this work provide a new insight in the fundamental understanding of shock waves in porous media. **In particular, a new scaling law relating the shock width to the initial void radius is obtained when micro-inertia effects are significant.**

*Corresponding author

Email addresses: christophe.czarnota@univ-lorraine.fr (Christophe Czarnota),
alain.molinari@univ-lorraine.fr (Alain Molinari),
sebastien.mercier@univ-lorraine.fr (Sébastien Mercier)

Keywords: shock waves, porous material, inertia effects

1. Introduction

1.1. Background: Shock in porous metallic materials

Shock waves in porous materials are of primary importance in numerous fields whether it concerns optimization of blast mitigation devices, collision processes in the solar system, clinical applications such as kidney stones fragmentation by shock wave lithotripsy. Porous materials generally contain voids with various initial sizes and shapes. Under rapid loading, micro-acceleration fields are developed around void boundaries due to the fast void growth/collapse. These local acceleration forces, that are referred to as micro-inertia effects, may play a crucial role in the void volume change. In this paper, a theoretical approach is proposed aiming at developing a comprehensive understanding of the effect of micro-inertia in steady shock wave propagation in ductile porous metallic materials.

The formation of steady shock waves in nonlinear heterogeneous materials reveals particular aspects that have been deeply investigated in Knowles (2002) for rubberlike materials. For these materials under tensile loading, the stress is a concave increasing function of strain in the low strain range and becomes strongly convex for large strains. The author then discussed the validity of possible shock formation in this family of materials.

The role of porosity on the occurrence of a steady plastic shock wave in porous media has been addressed in Cohen & Durban (2015). The authors considered finite strain and a matrix material following a Hookean hypoelastic law. Strain hardening was also included in the plastic response of the matrix through a Gurson-Tvergaard-Needleman (GTN) flow surface. Notably, it was shown that the critical impact velocity associated to the formation of a steady shock wave is a non monotonic function of the initial porosity.

Phenomenological approaches have first emerged to describe and identify the dynamic response of porous solids under shock. The P- α model, developed by Herrmann (1969) for use in hydrodynamic codes is founded on the introduction of a parameter, α ,

in the equation of state of the porous material, defined as the ratio of the specific volume of the porous material to that of the matrix material. This enables to separate the effects of void collapse and compression of matrix material. The P - α model has shown good accuracy in reproducing experimental Hugoniot data for iron and aluminium with various initial porosities. The equation of state in Herrmann (1969) must be completed by a relationship describing the evolution of α . Empirical void collapse laws were generally used up to the approach developed in Carroll & Holt (1972). Using the hollow sphere model, these authors have proposed an analytical void collapse law including micro-inertia effects. The case of a pure hydrostatic loading was considered and the pressure was found to be the sum of an inertia-dependent part and a quasistatic contribution. The matrix material was assumed to be elastic perfectly plastic. The change of porosity due to elasticity was shown to be small. Butcher et al. (1974), revisiting the version of Carroll & Holt (1972), have raised that deviatoric stresses cannot be neglected, contrary to what is usually assumed in most wave propagation modelings. The authors particularly highlighted that an increase of the initial void radius leads to a reduction in the rate of change of particle velocity in the steady wave profile. The same applies when increasing the viscous sensitivity. Micro-inertia is then shown to bring a rate dependency that acts in a similar way as viscosity does on the void collapse process. Both micro-inertia and viscosity tend to delay the void evolution.

Founded on the approach of Carroll & Holt (1972), numerous works have been dedicated to spall fracture so that tensile loadings rather than compressive have been considered. Main effects of micro-inertia and viscosity observed in compressive loadings are preserved in tensile loadings. In this context, Johnson (1981) has proposed a modeling including micro-inertia effects and a linear viscous dependence of the matrix behavior. The author found that plastic flow dominates the void growth rather than micro-inertia (at least in some specific cases). This result, governed by the way viscous effects are accounted for, may have oriented many further researches on dynamic ductile behavior. Carroll et al. (1986) have also assumed a large strain rate sensitivity in the dynamic void collapse but have adopted temperature dependence of the yield strength and viscosity. The relative importance of viscous and micro-inertia effects is highlighted. It is notably shown that micro-inertia becomes dominant in the tempera-

60 ture dependent case, as strength and viscosity decrease with temperature rise.

The dynamic expansion of an isolated void in a viscoplastic matrix, addressed by Ortiz & Molinari (1992), has revealed useful insights into the role of micro-inertia. Adopting a power-law potential to describe the matrix behavior, these authors found that the early stage of void growth is controlled by viscoplastic and strain-hardening
65 properties of the matrix whereas the late stage is dominated by micro-inertia. The interplay between viscous and micro-inertia effects was also studied in Molinari & Mercier (2001). In that work, the hollow sphere model was adopted to derive a micro-mechanical modeling accounting for micro-inertia and viscoplasticity. The authors found that the macroscopic stress tensor has two contributions: a quasistatic part, that
70 can be derived from a quasistatic viscoplastic flow potential or flow surface, and a micro-inertia contribution. This modeling has been used in Czarnota et al. (2006) and Czarnota et al. (2008) to describe spall fracture in a high purity grade tantalum and successfully reconstitute experimental free surface velocity profiles for various plate impact configurations. The modeling was completed in Jacques et al. (2010) by the use
75 of a Mie Gruneisen equation of state to describe the nonlinear elastic behavior of the material. In that work, the modeling was able to reconstitute free surface velocity profiles, but also to satisfactorily depict experimental measures of the damage distribution in impacted samples. Theoretical predictions of damage evolution were shown to be significantly affected by micro-inertia. Recently, Barthélémy et al. (2016) have integrated
80 micro-inertia in the modeling of acoustic and shock wave propagation in closed-cell foams. The authors have shown that the model with micro-inertia is able to reproduce accurately the wave profile identified from conducted 3D FEM calculations. Our goal is different since we focus only on material with **relatively low porosity (less than 0.3)** to investigate the effect of the material internal structure (void size, porosity) on the
85 shock structure. The response of materials with low porosity is quite different from foams and a fully deductive analytical modeling can be developed.

The plastic shock width is a particular characteristic of steady shock waves which was investigated by Dunin & Surkov (1979) by using the classical hollow sphere model with hydrostatic loading. The micro-inertia contribution (based on the Carroll & Holt,
90 1972, approach) and the influence of viscous effects were accounted for in the overall

response of the porous medium. When viscosity is neglected, the shock width is found to be determined mainly by the geometry of the void irrespective of the magnitude of the shock pressure. This may be the consequence of the influence of the void radius on micro-inertia effects. Kiselev (1995) has considered porous aluminium on the basis of a mathematical model accounting for plasticity and viscoplasticity of the matrix material. 95 The model was applied to explore the effect of porosity observed in the experiments of Butcher et al. (1974) on porous Al2024. Calculations for dense Al2024 were additionally conducted in Kiselev (1995) for comparison. It was shown that porosity results in a significant decrease in the shock wave velocity and that the shock width (estimated 100 from the time to void closure) is larger in porous materials. This result should be put in perspective. The definition of the shock width from the work of Kiselev (1995) has a meaning for porous media that is lost when dealing with dense materials. Therefore comparison should be interpreted with care. Other definitions of the shock width can be found in the literature. In the work of Butcher et al. (1972), the steady shock wave 105 width is defined from the ratio between the compaction wave amplitude to the maximum value of the stress gradient in the steady wave front. In the work of Molinari & Ravichandran (2004) dealing with dense aluminium 6061, the shock width is defined as the ratio of the accumulated plastic strain behind the shock to the maximum value of the plastic strain gradient in the steady plastic wave front. This type of characterization 110 appears to be consistent when considering both porous and dense materials.

1.2. Objectives and scope

The present study proposes a theoretical approach which integrates a coupling of micro-inertia with viscoplasticity effects. It aims at exploring the structure of steady shocks in porous ductile metallic materials. The matrix surrounding voids does not be- 115 have as a Bingham plasticity model, as it is usually found in the literature for describing high rate behavior (e.g. Dunin & Surkov, 1979). The constitutive framework of Molinari & Ravichandran (2004) developed for dense metals is extended to porous metals with the objective of analyzing the effects of initial porosity and void radii. Our approach is exemplified on porous aluminium with a specific emphasis on micro-inertia 120 effects generated near collapsing voids, Czarnota et al. (2016). The matrix material,

corresponding to the dense aluminium 6061-T6 considered in Molinari & Ravichandran (2004) is assumed nonlinear elastic and viscoplastic, exhibiting strain hardening. The rate dependency of the matrix material adopted in our work is consistent with the nonlinear viscous dependence of the dense material.

125 The outline of this paper is as follows. In section 2.1, we present the kinematics and field equations governing the propagation of steady plane shock waves in porous media. The matrix material behavior and the porous medium response, based on a GTN flow surface and including micro-inertia, are described. Section 3 focuses on the steady shock wave itself. Considering [shocks up to 8GPa](#), quasistatic compression curves are used to define the shock path with a chord criterion. Then, follows the analysis of the shock structure with a characterization of the shock width. Section 4 illustrates the effect of porosity and highlights the influence of void size on the shock structure. The shock wave is shown to be significantly structured by micro-inertia effects. The shock width turns out to be closely related to the internal structure of the porous medium and appears to be scaled by the initial void radius when micro-inertia effects are significant. [A new scaling law, accounting for combined effects of material properties and micro-inertia is then proposed.](#) These results are compared to those of [Carroll et al. \(1986\)](#) obtained in the case where the shock structure is solely governed by [micro-inertia effects](#). The paper closes with Section 5 presenting conclusions.

140 2. Framework

2.1. Kinematics of the porous medium

Let us consider a planar impact experiment on a porous sample of initial porosity f_0 [containing an isotropic distribution of a homogeneous population of voids of initial radius \$a_0\$.](#) Fig. 1 illustrates the corresponding homogeneous equivalent medium [impacted in the longitudinal direction \$\mathbf{e}_1\$.](#) The sample is assumed of sufficient length [so that the shock wave becomes steady beyond a certain propagation distance.](#) The matrix material of initial mass density ρ_{0m} is assumed nonlinear elastic/viscoplastic. Microscopic and macroscopic material responses are assumed to be isotropic. Note that stresses, stretches and strains introduced in this subsection 2.1 are macroscopic

150 quantities for the voids/matrix composite material. Due to the large deformations encountered in shock experiments, a Lagrangian formulation is adopted and we denote by X the Lagrangian coordinate in the initial configuration and in the direction of wave propagation. The current position of the material particle is denoted x and the longitudinal displacement is $u(X, t) = x - X$. The kinematic is that of uniaxial compression. The resulting deformation gradient tensor is expressed in the orthonormal frame $(\mathbf{e}_1, \mathbf{e}_2, \mathbf{e}_3)$, see Fig. 1, as:

$$\mathbf{F} = \lambda_1(X, t)\mathbf{e}_1 \otimes \mathbf{e}_1 + \mathbf{e}_2 \otimes \mathbf{e}_2 + \mathbf{e}_3 \otimes \mathbf{e}_3 \quad (1)$$

where \otimes stands for the outer product. $\lambda_1(X, t)$ is the longitudinal stretch defined by:

$$\lambda_1(X, t) = \frac{\partial x}{\partial X} = 1 + \frac{\partial u(X, t)}{\partial X} = \frac{dV}{dV_0} = \det(\mathbf{F}), \quad (2)$$

where dV and dV_0 denote the current and the initial volume of the particle of porous medium. The term $\det(\bullet)$ stands for the determinant of the tensor \bullet . For convenience, dependencies in X and t are intentionally omitted in the following. Using the standard multiplicative decomposition, the deformation gradient can be decomposed into elastic and plastic parts:

$$\mathbf{F} = \mathbf{F}^e \mathbf{F}^p, \quad (3)$$

where

$$\mathbf{F}^e = \lambda_1^e \mathbf{e}_1 \otimes \mathbf{e}_1 + \lambda_2^e (\mathbf{e}_2 \otimes \mathbf{e}_2 + \mathbf{e}_3 \otimes \mathbf{e}_3), \quad (4)$$

$$\mathbf{F}^p = \lambda_1^p \mathbf{e}_1 \otimes \mathbf{e}_1 + \lambda_2^p (\mathbf{e}_2 \otimes \mathbf{e}_2 + \mathbf{e}_3 \otimes \mathbf{e}_3). \quad (5)$$

165 λ_i^e (resp. λ_i^p), $i = 1, 2$, stand for elastic (resp. plastic) stretches aligned with the direction e_i . The porosity evolution during elastic loading is assumed negligible and the matrix is considered plastically incompressible. Under such considerations, components of the elastic \mathbf{F}^e and plastic \mathbf{F}^p deformation gradients can be expressed in terms of initial and current porosities, resp. f_0 and f , plastic and total longitudinal stretches, resp. λ_1^p and λ_1 :

$$\lambda_1^e = \frac{\lambda_1}{\lambda_1^p}, \lambda_2^e = \left(\frac{1-f_0}{1-f} \right)^{-1/2} (\lambda_1^p)^{1/2}, \lambda_2^p = \left(\frac{1-f_0}{1-f} \right)^{1/2} (\lambda_1^p)^{-1/2}. \quad (6)$$

2.2. Stress and strain rate tensors

For planar shocks, the first Piola Kirchhoff stress tensor \mathbf{T} is axisymmetric:

$$\mathbf{T} = T_1 \mathbf{e}_1 \otimes \mathbf{e}_1 + T_2 (\mathbf{e}_2 \otimes \mathbf{e}_2 + \mathbf{e}_3 \otimes \mathbf{e}_3). \quad (7)$$

The Cauchy stress tensor Σ is related to \mathbf{T} by:

$$\mathbf{T} = \Sigma J \mathbf{F}^{-\mathbf{T}}, \text{ with } J = \det(\mathbf{F}). \quad (8)$$

175 Thus Σ can be written as follows:

$$\Sigma = T_1 \mathbf{e}_1 \otimes \mathbf{e}_1 + \frac{T_2}{\lambda_1} (\mathbf{e}_2 \otimes \mathbf{e}_2 + \mathbf{e}_3 \otimes \mathbf{e}_3), \quad (9)$$

The Cauchy mean stress is therefore given by:

$$\Sigma_m = \text{tr}(\Sigma)/3 = \frac{1}{3} \left(T_1 + 2 \frac{T_2}{\lambda_1} \right), \quad (10)$$

where tr denotes the trace operator. Since $\Sigma_{11} - \Sigma_{22}$ is negative in compressive loading, the equivalent Cauchy stress is given by:

$$\Sigma_{\text{eq}} = \sqrt{\frac{3}{2} \Sigma' : \Sigma'} = |\Sigma_{11} - \Sigma_{22}| = \Sigma_{22} - \Sigma_{11} = \frac{T_2}{\lambda_1} - T_1, \quad (11)$$

180 where $(:)$ denotes the twice contracted product of second order tensors and Σ' stands for the deviatoric part of Σ . We shall use later the following definition of the compression stress:

$$\sigma = -T_1 > 0. \quad (12)$$

From Eqs (5-6), the macroscopic plastic strain rate $\mathbf{D}^p = \dot{\mathbf{F}}^p \mathbf{F}^{-p}$ is expressed as:

$$\mathbf{D}^p = \frac{\dot{\lambda}_1^p}{\lambda_1^p} \mathbf{e}_1 \otimes \mathbf{e}_1 - \frac{1}{2} \left(\frac{\dot{\lambda}_1^p}{\lambda_1^p} - \frac{\dot{f}}{1-f} \right) (\mathbf{e}_2 \otimes \mathbf{e}_2 + \mathbf{e}_3 \otimes \mathbf{e}_3), \quad (13)$$

where the overdot stands for the time derivative operator. From Eq. (13), the mean plastic strain rate $D_m^p = \frac{1}{3} \text{tr}(\mathbf{D}^p)$ is:

$$D_m^p = \frac{\dot{f}}{3(1-f)}. \quad (14)$$

185 Obviously, Eq. (14) represents the classical evolution law for f when the elastic contribution of porosity change is negligible. Denoting $\mathbf{D}^{p'}$ the deviatoric part of \mathbf{D}^p , the equivalent plastic strain rate is:

$$D_{\text{eq}}^p = \sqrt{\frac{2}{3} \mathbf{D}^{p'} : \mathbf{D}^{p'}} = \left| \frac{\dot{\lambda}_1^p}{\lambda_1^p} - D_m^p \right| = -\frac{\dot{\lambda}_1^p}{\lambda_1^p} + D_m^p \quad (15)$$

since, using the viscoplastic flow rule detailed in the forthcoming section, one can show that the sign of $\dot{\lambda}_1^p/\lambda_1^p - D_m^p$ is negative.

190 2.3. Field equations

In its Lagrangian form, the conservation of linear momentum for the porous medium reads:

$$\frac{\partial T_1}{\partial X} = \rho_{0m}(1-f_0) \frac{\partial v}{\partial t}, \quad (16)$$

where t is time and $v = \frac{\partial u(X,t)}{\partial t}$ is the particle velocity. The equation of compatibility provides the additional relation:

$$\frac{\partial v}{\partial X} = \frac{\partial \lambda_1}{\partial t}. \quad (17)$$

During shock experiments, the stress level can reach several GPa in compression. For such levels of stress, nonlinear elasticity has to be integrated in the modeling. This is done at the scale of the porous material based on the internal strain energy proposed by Clifton (1970) for dense aluminium material and modified here to take into account the influence of porosity. The first Piola Kirchhoff stress tensor components of the porous medium are expressed as:

$$T_1 = \frac{\rho_{0m}(1-f_0)}{\lambda_1^p} (1-f) F_1(\varepsilon_1^e, \varepsilon_2^e), \quad (18a)$$

$$\begin{aligned} T_2 &= \frac{\rho_{0m}(1-f_0)}{\lambda_2^p} (1-f) F_2(\varepsilon_1^e, \varepsilon_2^e) \\ &= \rho_{0m} [(1-f_0)(1-f)^3 \lambda_1^p]^{1/2} F_2(\varepsilon_1^e, \varepsilon_2^e), \end{aligned} \quad (18b)$$

where ε_1^e and ε_2^e are the elastic deformation components:

$$\varepsilon_1^e = \lambda_1^e - 1 = \frac{\lambda_1}{\lambda_1^p} - 1, \quad (19a)$$

$$\varepsilon_2^e = \lambda_2^e - 1 = \frac{1}{\lambda_2^p} - 1 = \left(\frac{1-f_0}{1-f} \right)^{-1/2} (\lambda_1^p)^{1/2} - 1. \quad (19b)$$

195 Derivation of Eqs (18) and (19) are provided in [Supplementary Material](#). The functions $F_i(\varepsilon_1^e, \varepsilon_2^e)$, ($i = 1, 2$) are solely related to elastic strains:

$$F_i(\varepsilon_1^e, \varepsilon_2^e) = A_{i1}\varepsilon_1^e + A_{i2}\varepsilon_1^{e2} + B_{i1}\varepsilon_2^e + B_{i2}\varepsilon_2^{e2} + D_i\varepsilon_1^e\varepsilon_2^e, \quad (20)$$

with

$$\begin{aligned} A_{11} &= 2a_2, & A_{12} &= 3a_4, \\ B_{11} &= 4a_2 + 2a_3, & B_{12} &= 12a_4 + 5a_5 + a_6, \\ D_1 &= 12a_4 + 4a_5, \end{aligned} \quad (21)$$

$$\begin{aligned} A_{21} &= 2a_2 + a_3, & A_{22} &= 3a_4 + a_5, \\ B_{21} &= 4a_2 + a_3, & B_{22} &= 12a_4 + 3a_5, \\ D_2 &= 12a_4 + 5a_5 + a_6. \end{aligned}$$

Second and third-order elastic constants a_i are involved in $F_i(\varepsilon_1^e, \varepsilon_2^e)$, ($i = 1, 2$). They have been characterized by ultrasonic measurements to describe the nonlinear elastic response of dense aluminium, see Clifton (1970) and Table 1. Note that the constitutive hypotheses made here will be validated against experimental results, when
200 considering the relationship between shock velocity and particle velocity, see Fig. 4.

Next, the description of the matrix behavior follows the work of Molinari & Ravichandran (2004) and is inherited from the dislocation based modeling proposed by Clifton (1970). Let's define

$$\gamma^p = \int \Phi dt, \quad (22)$$

205 as a measure of the plastic shear strain within the matrix domain. Φ is the rate at which plasticity accumulates (as the consequence of the movement, generation and annihilation of dislocations) and is governed by an Orowan type relation:

$$\Phi = bN\bar{v}, \quad (23)$$

where b is a constant (the Burgers vector). The expressions for the mobile dislocation density $N = N(\gamma^p)$ and the average dislocation velocity $\bar{v} = \bar{v}(\bar{\sigma}, \gamma^p)$, $\bar{\sigma}$ being an

210 average effective stress in the matrix, are taken from Clifton (1970) (the temperature dependence of N and \bar{v} is disregarded here):

$$N(\gamma^p) = N_{m0} \left(1 + \frac{\alpha_b \gamma^p}{b N_{t0}} \right) \exp(-\alpha_t \alpha_b \gamma^p), \quad (24)$$

where N_{m0} is the initial mobile dislocation density, N_{t0} is the initial total dislocation density, α_b is the breeding coefficient and α_t is the trapping coefficient.

The velocity \bar{v} is given in terms of the stress $\bar{\sigma}$ and the accumulated plastic shear strain 215 γ^p by an overstress model:

$$\bar{v}(\bar{\sigma}, \gamma^p) = c_1 \left(\frac{\langle F_\sigma \rangle}{2T_1^*} \right)^M \quad (25)$$

with $\langle F_\sigma \rangle = 0$ when $F_\sigma \leq 0$ and $\langle F_\sigma \rangle = F_\sigma$ when $F_\sigma \geq 0$.

The overstress function F_σ is:

$$F_\sigma = \bar{\sigma} - \bar{\sigma}_a, \quad (26)$$

where $\bar{\sigma}_a$ is the rate-independent yield strength of the matrix. T_1^* , c_1 are parameters and M is the inverse of the strain rate sensitivity. Strain hardening is included and a 220 power law function is adopted to model the matrix yield strength $\bar{\sigma}_a$:

$$\bar{\sigma}_a = \sigma_{a0} \left[1 + \left(\frac{\gamma^p}{\gamma_0} \right)^{1/n} \right], \quad (27)$$

where σ_{a0} , γ_0 and n are material parameters.

Our goal is to investigate the effect of micro-inertia on the shock structure. So the previous model has to be completed with additional relationships. When the porous material undergoes rapid loading, the matrix material in the vicinity of voids sustains 225 large accelerations that have to be accounted for. In this paper, we consider [shock levels up to 8GPa](#) and temperature effects are disregarded in the modeling.

From the work of Molinari & Mercier (2001), the macroscopic stress tensor Σ has two contributions:

$$\Sigma = \Sigma^* + \Sigma^{\text{dyn}}. \quad (28)$$

Σ^{dyn} stands for the part accounting for micro-inertia effects. Σ^* includes the rheological response of the matrix material and is micro-inertia independent. Σ^* can be derived from any pertinent quasistatic viscoplastic potential or flow surface. When

micro-inertia effects are disregarded, $\Sigma^{\text{dyn}} = \mathbf{0}$ and $\Sigma = \Sigma^*$.

The present work is restricted to planar impacts of porous materials containing spherical voids. We consider the hollow sphere model consisting of a spherical void of initial radius a_0 embedded in a spherical shell of matrix material with initial porosity f_0 . Additionally, it is assumed that the voids remain spherical during collapse and that the dynamic stress is essentially spherical. This framework is valid for the high stress triaxiality encountered in plate impact experiments. Such an assumption has been used for plate impact tests and spall fracture in tantalum (see Czarnota et al., 2006, 2008; Jacques et al., 2010) and experimental data have been successfully restituted.

The present model, which is a particular case of the general modeling proposed in Molinari & Mercier (2001), is written as:

$$\Sigma_m = \Sigma_m^* + \rho_{0m} a^2 \left[\dot{D}_m^p \left(f^{-1} - f^{-2/3} \right) + (D_m^p)^2 \left(3f^{-1} - \frac{5}{2}f^{-2/3} - \frac{1}{2}f^{-2} \right) \right], \quad (29)$$

$$\Sigma' = \Sigma^{*'}, \quad \Sigma_{\text{eq}} = \Sigma_{\text{eq}}^*. \quad (30)$$

The second term of the right hand side of Eq. (29) corresponds to the theory proposed by Carroll & Holt (1972) for the dynamic compaction of powders. Micro-inertia effects are thus found to be scaled by the matrix mass density ρ_{0m} and the square of the current void radius a .

The radius a can be expressed in terms of initial porosity f_0 , initial void radius a_0 , and current porosity f as follows:

$$a = a_0 \left(\frac{1-f_0}{f_0} \right)^{1/3} \left(\frac{f}{1-f} \right)^{1/3}. \quad (31)$$

Substituting Eq. (31) in Eq. (29) and using Eq. (14) relating the mean plastic strain rate D_m^p to porosity f and its time derivative \dot{f} , Eq. (29) is a nonlinear equation containing the first and second derivatives of f :

$$\Sigma_m = \Sigma_m^* + \frac{\rho_{0m} a_0^2}{3} \left(\frac{1-f_0}{f_0} \right)^{2/3} \left[\frac{f^{-1/3} - 1}{(1-f)^{5/3}} \dot{f} + \frac{-\frac{1}{6}f^{-4/3} + 2f^{-1/3} - \frac{11}{6}}{(1-f)^{8/3}} \dot{f}^2 \right]. \quad (32)$$

The quasistatic stress $\Sigma^* = \Sigma^{*\prime} + \Sigma_m^* \mathbf{I}$ and the plastic strain rate \mathbf{D}^p are related by the flow law:

$$\mathbf{D}^p = \dot{\kappa} \frac{\partial \Omega(\Sigma^*)}{\partial \Sigma^*}, \quad (33)$$

240 where $\Omega = 0$ characterizes the flow surface; $\Omega(\Sigma^*)$ is given by classical homogenization approaches (without micro-inertia) and $\dot{\kappa}$ is the plastic multiplier subject with Ω to the Kuhn-Tucker complementary conditions: $\Omega \leq 0$, $\dot{\kappa} \geq 0$, $\Omega \dot{\kappa} = 0$ (Simo & Hughes, 1998).

We consider here the Gurson-Tvergaard-Needleman (GTN) based viscoplastic flow 245 surface (Gurson, 1977; Tvergaard, 1981; Needleman & Tvergaard, 1991):

$$\Omega(\Sigma^*, \bar{\sigma}, f) = \left(\frac{\Sigma_{\text{eq}}^*}{\bar{\sigma}} \right)^2 + 2q_1 f \cosh \left(\frac{3}{2} q_2 \frac{\Sigma_m^*}{\bar{\sigma}} \right) - [1 + (q_1 f)^2] = 0. \quad (34)$$

The plastic work rate of the porous medium is set equal to the matrix dissipation rate:

$$\Sigma^* : \mathbf{D}^p = \Sigma_{\text{eq}}^* D_{\text{eq}}^p + 3\Sigma_m^* D_m^p = (1-f) \bar{\sigma} \dot{\epsilon}_{\text{eq}}^p, \quad (35)$$

where $\dot{\epsilon}_{\text{eq}}^p$ is the von Mises equivalent plastic strain rate in the matrix (Needleman et al., 1992) related to Φ by:

$$\dot{\epsilon}_{\text{eq}}^p = \frac{2\Phi}{3}. \quad (36)$$

Then, from Eqs (10-11,14-15, 33-36), one has:

$$\frac{\dot{\lambda}_1^p}{\lambda_1^p} = - \frac{(1-f) \Phi \left[\frac{2\Sigma_{\text{eq}}^*}{\bar{\sigma}} + q_1 q_2 f \sinh \left(-\frac{3}{2} q_2 \frac{\Sigma_m^*}{\bar{\sigma}} \right) \right]}{3 \left[\left(\frac{\Sigma_{\text{eq}}^*}{\bar{\sigma}} \right)^2 + \frac{3\Sigma_m^*}{2\bar{\sigma}} q_1 q_2 f \sinh \left(\frac{3}{2} q_2 \frac{\Sigma_m^*}{\bar{\sigma}} \right) \right]} \quad (37)$$

250 and

$$\frac{\dot{f}}{1-f} = - \frac{(1-f) \Phi q_1 q_2 f \sinh \left(-\frac{3}{2} q_2 \frac{\Sigma_m^*}{\bar{\sigma}} \right)}{\left(\frac{\Sigma_{\text{eq}}^*}{\bar{\sigma}} \right)^2 + \frac{3\Sigma_m^*}{2\bar{\sigma}} q_1 q_2 f \sinh \left(\frac{3}{2} q_2 \frac{\Sigma_m^*}{\bar{\sigma}} \right)}. \quad (38)$$

The problem of propagation of steady plastic waves in viscoplastic porous materials accounting for micro-inertia is therefore governed by Eqs (37-38) combined to Eqs (30) and (32). Recall that the present approach is developed for high stress triaxiality encountered in planar impacts for which Σ^{dyn} is approximately spherical and 255 $\Sigma_{\text{eq}} = \Sigma_{\text{eq}}^*$ is verified to a good approximation (see Eq. 30).

Once the porous material is totally densified, the viscoplastic flow is governed by

the von Mises flow theory. Such a situation (i.e $f_0 \neq 0$ and $f = 0$ after full densification) is addressed in Appendix A. In particular, it is shown that the modeling of Molinari & Ravichandran (2004), dedicated to initially dense materials, is retrieved
 260 from our approach.

3. Steady shock wave

During planar impact tests a stationary shock forms beyond a certain propagation distance, see Fig 1. For large amplitude shocks, the final states reached by material particles beyond the shock are determined from Hugoniot curves. In the case of weak
 265 shocks it is expected that temperature effects are limited. The present work mainly focuses on shocks of amplitudes lower than 8GPa and isothermal compression curves are used to define the post shock states instead of Hugoniot curves, thus following the same framework as Molinari & Ravichandran (2004).

3.1. Quasistatic compression curve

In this section, we concentrate on the quasistatic isothermal compression curve
 270 \mathcal{C}_Y which governs the rate independent response of the material (viscous effects and micro-inertia being disregarded due to slow loading). The quasistatic yield surface of the porous material is governed by the GTN rate independent yield function:

$$\Omega_a = \Omega(\Sigma, \bar{\sigma}_a, f) = \left(\frac{\Sigma_{eq}}{\bar{\sigma}_a}\right)^2 + 2q_1 f \cosh\left(\frac{3}{2}q_2 \frac{\Sigma_m}{\bar{\sigma}_a}\right) - [1 + (q_1 f)^2] = 0, \quad (39)$$

with $q_1 = q_2 = 1$ and $\bar{\sigma}_a$ given by Eq. (27). The rate independent response defining the isothermal compression curve \mathcal{C}_Y is obtained from Eqs (18-22), Eqs (33-35)
 275 and Eq. (39) after substituting $\bar{\sigma}$ by $\bar{\sigma}_a$ and Ω by Ω_a . Further details about the construction of the compression curve \mathcal{C}_Y are provided in Supplementary Material. As in Clifton (1970) and Molinari & Ravichandran (2004), the matrix material is 6061-T6 aluminium. Material parameters referring to room temperature (25°C) and atmospheric
 280 pressure are given in Table 1.

Fig. 2 presents, for several initial porosities, quasistatic compression curves \mathcal{C}_Y which display the evolution of the compressive stress $\sigma = -T_1$ as a function of the

longitudinal stretch λ_1 . Compressive responses up to 8GPa are shown for dense ($f_0=0$) and porous aluminium. The initial porosity is ranging from 0.0003 to 0.1 ($f_0 = 0.0003, 0.003, 0.03, 0.1$). Fig. 2 gives a clear indication of the effect of initial porosity. For a given stress, a higher accumulated plastic strain is produced when f_0 is increased (because of the weakening of the yield limit due to porosity), so λ_1 is smaller. Besides, the case $f_0=0.0003$ is hardly distinguishable from that obtained when $f_0=0$, meaning that the proposed approach applied to very dilute porous material is consistent with the limiting case of a dense metal. Fig. 2 also reveals that porous materials exhibit the same elastic plastic behavior (revealed by the slope of the \mathcal{E}_Y curve) once the densification is achieved. As an indication, the state of full pore closure is identified by the symbol ∇ on Fig. 2 which marks the end of the densification process (defined here when the porosity is below 10^{-5}). Materials with higher initial porosity need higher stress to reach the full compacted state. This may be due to the strain hardening of the matrix material.

3.2. Shock path

For shock amplitudes up to the initial elastic limit, a pure elastic shock is triggered. For dense aluminium subjected to higher shock amplitudes, a first elastic wave (elastic precursor) compresses the material up to the initial elastic limit followed by a plastic wave that compresses further the material. The shock path (in the $\lambda_1 - \sigma$ plane) following the elastic precursor can be characterized as the line connecting the elastic limit state to the post-shock state that is located on the isothermal compression curve. This straight line, referred to as the Rayleigh line, can be defined without ambiguity for any compaction stress levels since the compression curve for dense aluminium presented in Fig. 2 is convex for all λ_1 beyond the elastic limit.

For porous aluminium, the situation is different. The isothermal compression curve presented in Fig. 3 shows an inflection point at (λ_1^0, σ^0) . The position of the inflection point depends on the initial porosity. In that case, the structure of the shock is more complex. The plastic shock structure consists of a fan followed by a shock wave and the identification of the dynamic path relies on the chord criterion (Knowles, 2002; Făciu & Molinari, 2006). In the case of compressive loading, the chord criterion is

fulfilled if and only if the chord lies above the graph of $\sigma(\lambda_1)$ in the $(\lambda_1 - \sigma)$ plane.

Let's denote by (e) the state of initial yielding, see Fig. 3. The state reached at the rear of the fan structure will be referred to as state (+). The tangent to the compression curve \mathcal{C}_Y at state (+) defines the Rayleigh line which characterizes the shock path in the $(\lambda_1 - \sigma)$ plane. We denote by (λ_1^-, σ^-) the intersection of the Rayleigh line with \mathcal{C}_Y , see Fig. 3. By state (-) we refer to the material state reached at (λ_1^-, σ^-) by shock loading. For further comments on the characterization of material states we refer to Supplementary Material.

From previous comments, a plastic shock wave can be formed only for $\sigma^- > \sigma^0$, where σ^0 refers to the inflection point on the curve \mathcal{C}_Y . We note that by construction the chord criterion is satisfied and that the following condition is fulfilled at the point (λ_1^+, σ^+) :

$$\frac{T_1^- - T_1^+}{\lambda_1^- - \lambda_1^+} = -\frac{\sigma^- - \sigma^+}{\lambda_1^- - \lambda_1^+} = -\frac{d\sigma_{\mathcal{C}}}{d\lambda_1}(\lambda_1^+), \quad (40)$$

where we have denoted by $\sigma = \sigma_{\mathcal{C}}(\lambda_1)$ the stretch-stress relationship along the compression curve \mathcal{C}_Y .

It is worth noting that the Rayleigh line is defined from state (+) and state (-) or equivalently from state (+) and the slope $\frac{d\sigma_{\mathcal{C}}}{d\lambda_1}(\lambda_1^+)$, since there is a one-to-one correspondence between state (-) and $\frac{d\sigma_{\mathcal{C}}}{d\lambda_1}(\lambda_1^+)$. Note also that a straight path that would originate from state (e) to reach state (-) (with $\sigma^- > \sigma^0$) will cross \mathcal{C}_Y two times, thus violating the chord criterion and providing a non admissible solution. This path is indicated by a red dashed line on Fig. 3. The stretch level λ_1^0 beyond which a shock wave may occur depends on the initial porosity while λ_1^+ depends both on porosity and stress amplitude σ^- . In the case of high compressive stress level or for very dilute porous materials (small f_0), λ_1^+ tends to the elastic limit λ_1^e . Table 2 summarizes values of λ_1^e , σ^e , λ_1^0 and σ^0 (independent of σ^-) defining the elastic limit and inflection points for porous aluminium. Various initial porosities are tested. Values of λ_1^+ , σ^+ are also calculated for two levels of σ^- , 3 and 8GPa. For dense metals, the state (+) coincides obviously with state (e).

340 3.3. Shock structure

We assume that the material is subjected to a shock wave of Lagrangian celerity C with respect to the reference configuration. By introducing the moving coordinate

$$\xi = X - Ct, \quad (41)$$

Eqs (16-17) become

$$\frac{dT_1}{d\xi} = -\rho_{0m}C(1-f_0)\frac{dv}{d\xi}, \quad (42)$$

$$\frac{dv}{d\xi} = -C\frac{d\lambda_1}{d\xi}. \quad (43)$$

By integration with respect to ξ from state (+), the stress, particle velocity and stretch at any point within the plastic shock layer are [related by the following relationships](#):

$$T_1 - T_1^+ = -\rho_{0m}C(1-f_0)(v - v^+), \quad (44)$$

$$v - v^+ = -C(\lambda_1 - \lambda_1^+). \quad (45)$$

The combination of Eqs (44) and (45) provides a linear relation between stress T_1 and stretch λ_1 defining the Rayleigh line:

$$T_1 - T_1^+ = \rho_{0m}C^2(1-f_0)(\lambda_1 - \lambda_1^+). \quad (46)$$

As discussed in Section 3.2, the Rayleigh line is tangent to the compression curve \mathcal{C}_Y at state (+) and intersects \mathcal{C}_Y at state (-) characterized by (λ_1^-, σ^-) .

We investigate the steady shock structure from state (+) to state (-). Eqs (44-46) are in particular valid for state (-):

$$T_1^- - T_1^+ = -\rho_{0m}C(1-f_0)(v^- - v^+), \quad (47a)$$

$$v^- - v^+ = -C(\lambda_1^- - \lambda_1^+), \quad (47b)$$

$$T_1^- - T_1^+ = \rho_{0m}C^2(1-f_0)(\lambda_1^- - \lambda_1^+). \quad (47c)$$

345 Combining Eqs (40) and (47c), we get:

$$\frac{d\sigma_{\mathcal{C}}}{d\lambda_1}(\lambda_1^+) = -\rho_{0m}C^2(1-f_0). \quad (48)$$

For a given value of the shock speed C , λ_1^+ is determined from Eq. (48) and λ_1^- is solution of Eq. (47c) which can be written as:

$$-\sigma_{\mathcal{E}}(\lambda_1^-) + \sigma_{\mathcal{E}}(\lambda_1^+) = \rho_{0m} C^2 (1 - f_0) (\lambda_1^- - \lambda_1^+) . \quad (49)$$

Conversely, assuming that σ^- is given, then λ_1^- is obtained from $\sigma^- = \sigma_{\mathcal{E}}(\lambda_1^-)$ and λ_1^+ is solution of Eq. (40) where $\sigma^+ = \sigma_{\mathcal{E}}(\lambda_1^+)$. Finally, C is obtained from Eq. (47c). Because of the one-to-one correspondence between σ^- and C , it is equivalent to characterize a shock by its celerity or the stress level at state (-).

Let's remind that state (+) may differ from the initial yielding state (e) because of the evolution of porosity and plastic stretch along the fan, see Table 2. It is assumed that viscous and micro-inertia effects play no role in the fan structure so that both contributions are ignored in the determination of quantities at state (+). From state (e) to state (+), covering the fan structure, values of T_1 and λ_1 are gradually changed following the compression curve \mathcal{C}_Y . Stress and stretch at state (+) have been determined above. Evolutions of the plastic stretch and porosity can be evaluated along the isothermal compression curve from state (e) to state (+) (see Section 3.1 and Table 2). Besides, using Eqs (42-43) where C is replaced by the instantaneous fan velocity $\sqrt{\frac{dT_1/d\lambda_1}{\rho_{0m}(1-f_0)}}$, the corresponding particle velocity v^+ is obtained:

$$v^+ = v^e - \int_{(\text{e})}^{(+)} \sqrt{\frac{dT_1/d\lambda_1}{\rho_{0m}(1-f_0)}} d\lambda_1 , \quad (50)$$

where $\frac{dT_1}{d\lambda_1} = -\frac{d\sigma_{\mathcal{E}}}{d\lambda_1}(\lambda_1)$ is evaluated along the isothermal compression curve \mathcal{C}_Y . v^e is the particle velocity due to the elastic shock obtained from relationships similar to Eqs (42-43):

$$v^e = C^e (1 - \lambda_1^e) , \quad (51)$$

$$C^e = \sqrt{\frac{-T_1^e}{\rho_{0m}(1-f_0)(1-\lambda_1^e)}} , \quad (52)$$

with C^e being the elastic wave velocity. The elastic state and corresponding values of λ_1^e and $-T_1^e$ are identified from Eqs (18-20) and (39) with $f = f_0$, $\bar{\sigma}_a = \sigma_{a0}$, $\varepsilon_1^e = \lambda_1^e - 1$ and $\varepsilon_2^e = 0$. The knowledge of state (e) gives a clear definition of v^+ .

Once the states (+) and (-) are identified, the shock structure is obtained from a

nonlinear system of differential equations. When micro-inertia is disregarded, the nonlinear system is deduced from Eqs (22) and (37-38) with $\Sigma_{\text{eq}}^* = \Sigma_{\text{eq}}$, $\Sigma_{\text{m}}^* = \Sigma_{\text{m}}$:

$$\gamma_{,\xi}^{\text{p}} = -\frac{\Phi(\gamma^{\text{p}}, \bar{\sigma})}{C}, \quad (53a)$$

$$\lambda_{1,\xi}^{\text{p}} = \frac{\lambda_1^{\text{p}} (1-f) \Phi(\gamma^{\text{p}}, \bar{\sigma}) \left[\frac{2\Sigma_{\text{eq}}}{\bar{\sigma}} + q_1 q_2 f \sinh\left(-\frac{3}{2} q_2 \frac{\Sigma_{\text{m}}}{\bar{\sigma}}\right) \right]}{3C \left[\left(\frac{\Sigma_{\text{eq}}}{\bar{\sigma}}\right)^2 + \frac{3\Sigma_{\text{m}}}{2\bar{\sigma}} q_1 q_2 f \sinh\left(\frac{3}{2} q_2 \frac{\Sigma_{\text{m}}}{\bar{\sigma}}\right) \right]}, \quad (53b)$$

$$f_{,\xi} = \frac{(1-f)^2 \Phi(\gamma^{\text{p}}, \bar{\sigma}) q_1 q_2 f \sinh\left(-\frac{3}{2} q_2 \frac{\Sigma_{\text{m}}}{\bar{\sigma}}\right)}{C \left[\left(\frac{\Sigma_{\text{eq}}}{\bar{\sigma}}\right)^2 + \frac{3\Sigma_{\text{m}}}{2\bar{\sigma}} q_1 q_2 f \sinh\left(\frac{3}{2} q_2 \frac{\Sigma_{\text{m}}}{\bar{\sigma}}\right) \right]}. \quad (53c)$$

In presence of micro-inertia, Eqs (22, 32, 37) are used:

$$\gamma_{,\xi}^{\text{p}} = -\frac{\Phi(\gamma^{\text{p}}, \bar{\sigma})}{C}, \quad (54a)$$

$$\lambda_{1,\xi}^{\text{p}} = \frac{\lambda_1^{\text{p}} (1-f) \Phi(\gamma^{\text{p}}, \bar{\sigma}) \left[\frac{2\Sigma_{\text{eq}}^*}{\bar{\sigma}} + q_1 q_2 f \sinh\left(-\frac{3}{2} q_2 \frac{\Sigma_{\text{m}}^*}{\bar{\sigma}}\right) \right]}{3C \left[\left(\frac{\Sigma_{\text{eq}}^*}{\bar{\sigma}}\right)^2 + \frac{3\Sigma_{\text{m}}^*}{2\bar{\sigma}} q_1 q_2 f \sinh\left(\frac{3}{2} q_2 \frac{\Sigma_{\text{m}}^*}{\bar{\sigma}}\right) \right]}, \quad (54b)$$

$$f_{,\xi\xi} = \frac{3(\Sigma_{\text{m}} - \Sigma_{\text{m}}^*)}{\rho_{0\text{m}} a_0^2 C^2 \left(\frac{1-f_0}{f_0}\right)^{2/3}} (1-f)^{5/3} \left(f^{-1/3} - 1\right)^{-1} - f_{,\xi}^2 (1-f)^{-1} \left(f^{-1/3} - 1\right)^{-1} \left(2f^{-1/3} - \frac{1}{6}f^{-4/3} - \frac{11}{6}\right). \quad (54c)$$

where $\Sigma_{\text{eq}}^* = \Sigma_{\text{eq}}$, see Eq. (30). Moreover, it is important to mention that Eq. (38) is still satisfied, which in the moving coordinate system, leads to:

$$f_{,\xi} = \frac{(1-f)^2 \Phi(\gamma^{\text{p}}, \bar{\sigma}) q_1 q_2 f \sinh\left(-\frac{3}{2} q_2 \frac{\Sigma_{\text{m}}^*}{\bar{\sigma}}\right)}{C \left[\left(\frac{\Sigma_{\text{eq}}^*}{\bar{\sigma}}\right)^2 + \frac{3\Sigma_{\text{m}}^*}{2\bar{\sigma}} q_1 q_2 f \sinh\left(\frac{3}{2} q_2 \frac{\Sigma_{\text{m}}^*}{\bar{\sigma}}\right) \right]}. \quad (55)$$

The quantity $\bullet_{,\xi}$ (resp. $\bullet_{,\xi\xi}$) stands for the first (resp. second) derivative of \bullet with respect to ξ . The initial boundary conditions corresponding to state (+) are: $f(\xi = +\infty) = f^+$, $\lambda_1^{\text{p}}(\xi = +\infty) = \lambda_1^{\text{p}+}$, $\gamma^{\text{p}}(\xi = +\infty) = \gamma^{\text{p}+}$ and $f_{,\xi}(\xi = +\infty) = 0$. Recall that f^+ , $\lambda_1^{\text{p}+}$ and $\gamma^{\text{p}+}$ at state (+) are evaluated following the quasistatic response \mathcal{C}_Y from state (e) to state (+), see section 3.1. In addition, all states within the shock are constrained to remain on the Rayleigh line so that Eq. (46) is the fundamental equation for the shock structure problem.

The proposed modeling of steady shock waves in porous materials will bring useful information regarding the influence of micro-inertia and strain rate sensitivity on the shock profile. It has already been highlighted that both effects play a key role through their stabilizing effects (Butcher et al., 1974; Ortiz & Molinari, 1992; Molinari & Ravichandran, 2004; Weinberg & Ortiz, 2005). The evolution of the shock width, the maximum rate of change of quantities like stress level, plastic strain rate, particle velocity, plastic strain,... will appear as signatures of stabilizing effects of micro-inertia that are involved in the compaction process. As in Molinari & Ravichandran (2004) the shock width is defined from the variation of the equivalent plastic strain $\Delta E_{\text{eq}}^{\text{p}}$ within the shock layer:

$$w = \frac{\Delta E_{\text{eq}}^{\text{p}}}{\max\left(\left|\frac{dE_{\text{eq}}^{\text{p}}}{d\xi}\right|\right)}. \quad (56)$$

where $\Delta E_{\text{eq}}^{\text{p}} = E_{\text{eq}}^{\text{p}-} - E_{\text{eq}}^{\text{p}+}$. The accumulated plastic strain is defined as:

$$E_{\text{eq}}^{\text{p}} = \int_0^t D_{\text{eq}}^{\text{p}}(t') dt' \quad (57)$$

From Eqs (14) and (15) one obtains:

$$D_{\text{eq}}^{\text{p}} = C \left[\frac{\lambda_{1,\xi}^{\text{p}}}{\lambda_1^{\text{p}}} - \frac{f_{,\xi}}{3(1-f)} \right] = -C \frac{dE_{\text{eq}}^{\text{p}}}{d\xi} \quad (58)$$

Thus $\max\left(\left|\frac{dE_{\text{eq}}^{\text{p}}}{d\xi}\right|\right) = \frac{1}{C} \max(D_{\text{eq}}^{\text{p}})$ and by integration of Eq. (58) with respect to ξ from state (+) to state (-), the width becomes:

$$w = -\frac{C}{\max(D_{\text{eq}}^{\text{p}})} \ln \left[\frac{\lambda_1^{\text{p}-}}{\lambda_1^{\text{p}+}} \left(\frac{1-f^-}{1-f^+} \right)^{1/3} \right]. \quad (59)$$

4. Results and analysis

4.1. Plastic shock speed: comparison of modeling with experiments

In a first illustration of the model capability, we focus on the relationship between the plastic shock velocity C and the particle velocity v^- at state (-). This relationship is considered as a fundamental outcome of plate impact experiments. The quasistatic compression curve is first characterized. Then, for a fixed shock level σ^- , the corresponding stretch λ_1^- can be deduced. Based on the chord criterion (40), λ_1^+ and σ^+

are defined. The plastic shock wave velocity C is therefore obtained from Eq. (47c). Next, the GTN yield function (39) with $\bar{\sigma}_a = \sigma_0$ (the elastic yield limit) leads to the determination of the elastic limit (λ^e, σ^e). Then, the elastic wave speed C^e and particle velocity v^e are calculated (see Eqs. 51-52). Finally, the particle velocity v^- is computed from Eq. (47b) jointly with Eq. (50).

The predictions of the model (parameters listed in Table 1) are compared to experimental data of the literature. Fig. 4 shows the shock velocity C versus the particle velocity v^- . Experiments on porous aluminium alloys are depicted in terms of C versus v^{rear} data points where v^{rear} is the particle velocity behind the shock front. Parts of experimental data used for comparison are taken from Los Alamos Scientific Laboratory data available in Marsh (1980) where references of publications (if any) are also given. Different grades of aluminium were considered in experiments. It is interesting to notice that results are readily similar for the different grades. When available, aluminium grade is also indicated in Fig. 4. Iso- σ^- curves are shown as dashed lines. For a given shock level σ^- and a given aluminium alloy with initial porosity f_0 , the intersection of the corresponding dashed curve with the corresponding solid line gives the set (v^-, C) . It appears from Fig. 4 that the experimental data are satisfactorily described up to $\sigma^- = 30\text{GPa}$ for aluminium alloys in a large range of porosities. Let us remind that the temperature influence has been neglected in the proposed approach, such that application of the modeling is restricted to limited shock amplitudes. As a consequence, our approach appears to provide accurate predictions for shock stresses up to about 8GPa. The grey shaded area in Fig. 4 delimits the zone of interest addressed in the present work where we have used σ^- as the main shock intensity controller.

Besides, Fig. 4 also illustrates the effect of shock amplitude and porosity. It remarkably reveals the difference in the response between dense and porous materials, the contrast being much more marked for low shock amplitudes. For a given shock level, initial porosity induces a reduction in the shock wave velocity meaning that plastic shock waves will travel slowly in the porous media. This result confirms a recent analysis in the field of shock waves in porous materials, Cohen & Durban (2015). As an illustration, for $\sigma^- = 3\text{GPa}$, the shock velocity in the case of a material with $f_0 = 0.08$ is reduced by a factor $\simeq 1.8$ when compared to a dense material.

In the following, the joint effect of viscosity and micro-inertia on the shock structure is considered. Firstly, in section 4.2, we solely analyze the effect of viscosity by disregarding micro-inertia. In section 4.3 the micro-inertia contribution is added. This provides a clear understanding of both contributions.

4.2. Shock structure when disregarding micro-inertia

In order to rationalize the effect of porosity, results are first illustrated by neglecting micro-inertia effects on void collapse. The problem thus reduces to the set of nonlinear equations (53). In such a case, the initial void radius a_0 does not affect the response and only the initial porosity f_0 is influencing the plastic shock front for a given matrix behavior.

Results computed for various initial porosities ($f_0 = 0.0003, 0.003, 0.03, 0.1, 0.3$) are shown in Fig. 5 where the variation of the accumulated plastic strain E_{eq}^{p} with respect to position ξ is plotted for a stress amplitude of 3GPa leading to C varying in the range [2 146-5 514]m/s. The position $\xi = 0$ is defined as the locus exhibiting the maximum plastic strain rate, $\max(D_{\text{eq}}^{\text{p}})$, in the shock layer. As expected, it is observed in Fig. 5 that the very dilute case ($f_0 = 0.0003$) tends to the dense material case considered in Molinari & Ravichandran (2004). Another peculiarity concerns the sharpening of the shock front when f_0 is increased. As compared to dense materials, additional plasticity in porous media is activated due to void closure. Hence, the accumulated plastic strain $E_{\text{eq}}^{\text{p-}}$ in the rear of the shock increases for larger initial porosity. In addition, it is clearly shown from Fig. 5 that the shock width decreases when f_0 is increased.

Material particles are facing different plastic strain rates depending on the position within the shock. This is illustrated in Fig. 6 showing the evolution of D_{eq}^{p} versus ξ (semi-log scale) for the shock amplitude $\sigma^- = 3\text{GPa}$. For dense materials, the shock structure is symmetric with respect to $\xi=0$. For materials with low porosity, the porous medium is rapidly fully densified and the overall response mainly follows the dense material behavior. The strain rate profile is still highly symmetric. On the contrary, for materials with large porosity, a non symmetric profile with respect to $\xi=0$ is observed in Fig. 6. This is due to the densification process. Indeed, for larger initial porosities, the position $\xi = 0$ (where D_{eq}^{p} is maximum) approaches the rear of the shock front while

for dense and low porosity materials, (f_0 up to 0.003) $\xi=0$ is located approximately in the middle of the shock wave.

455 One observes also in Fig. 6 a rise in $\max(D_{\text{eq}}^{\text{p}})$ as f_0 is increased. From Eq. (58), where $D_{\text{eq}}^{\text{p}} = -C \frac{dE_{\text{eq}}^{\text{p}}}{d\xi}$, it appears that $\max(D_{\text{eq}}^{\text{p}})$ is controlled by two opposite effects when f_0 is increased: the reduction in C and the much higher values of $\max\left(\left|\frac{dE_{\text{eq}}^{\text{p}}}{d\xi}\right|\right)$ observed in Fig. 5. The value of the shock velocity C in porous aluminium roughly covers the range [2000-6000]m/s in the domain of investigation (see Fig. 4) while
 460 $\max\left(\left|\frac{dE_{\text{eq}}^{\text{p}}}{d\xi}\right|\right)$ is much more influenced by a variation in f_0 . As a consequence, $\max(D_{\text{eq}}^{\text{p}})$ is rather controlled by the strong change in $\max\left(\left|\frac{dE_{\text{eq}}^{\text{p}}}{d\xi}\right|\right)$. For example, $\max\left(\left|\frac{dE_{\text{eq}}^{\text{p}}}{d\xi}\right|\right) = 90974\text{m}^{-1}$ when $f_0=0.3$ and 68m^{-1} when $f_0=0.0003$. At the same time, the shock velocity is only increased by a factor 2.57.

In order to develop a better understanding of the non symmetric shock structure,
 465 the evolution of the porosity f vs ξ is superimposed to the evolution of D_{eq}^{p} in Fig. 7a for the case $f_0=0.03$ and $\sigma^- = 3\text{GPa}$ ($C=4059\text{m/s}$). Jointly, the evolution of D_{eq}^{p} with respect to the plastic strain E_{eq}^{p} is presented in Fig. 7b. A schematic illustration of three successive stages in the plasticity process is depicted in Fig. 7 based on the evolution of porosity and plastic deformation through the shock layer. It is confirmed that most part
 470 of the plastic strain is accumulated over stage II that corresponds to void closure and a decreasing of porosity. Stage I may be referred to as the response of a porous material with a near frozen porosity, while stage III stands for the response of the densified material. The symmetric/non symmetric characteristic of the shock wave is conditioned by the extent of stage II. For very low porosity, stage II is of a negligible size, leading
 475 to a highly symmetric shock structure.

To complete the analysis of the effect of porosity on shock waves in viscoplastic materials, Fig. 8 (semi-log scale) shows the evolution of the characteristic shock width w given by Eq. (59) in terms of the shock intensity σ^- for various initial porosities. Table 3 summarizes corresponding values of plastic shock velocities. The case of a
 480 dense material considered by Molinari & Ravichandran (2004) is also presented. It is seen that the proposed approach (micro-inertia disregarded) converges to the dense response when the initial porosity decreases to zero. It appears from Fig. 8 that for a

given shock level, the shock width is smaller as porosity increases and that a higher shock intensity also reduces the shock layer width.

485 4.3. Shock structure with micro-inertia effects

Before presenting the influence of micro-inertia on the shock structure and shock width, let us consider a given stress level σ^- and a given initial porosity f_0 . As described in Section 3.3, a unique plastic shock wave velocity C can be determined using the chord criterion and the quasistatic isothermal curve \mathcal{C}_Y . Equivalently, one can consider that C is given, to which is uniquely associated the stress level σ^- . The stress σ^- is related to the intersection (above σ^0) of the Rayleigh line with the quasistatic curve \mathcal{C}_Y . When micro-inertia is neglected, σ^- stands as the shock amplitude, i.e. equilibrium is reached at state (-). When micro-inertia is included, it appears that σ^- is not in general exactly the equilibrium stress σ^{rear} at the rear of the shock front since a residual microscale kinetic energy may still be present at state (-). The release of this residual kinetic energy may be responsible for oscillatory motion of collapsing pores. This stage will occur when the material is almost fully densified and will not change the shock structure in our approach (e.g. shock width, maximum plastic strain rate).

The construction of the entire shock path is not attempted here for the following reason: it will appear that most of the shock structure is obtained when the stress varies from σ^+ to σ^- , the evolution from σ^- to σ^{rear} having a marginal influence (see Fig. 12). Consequently, it is not crucial for the needs of this work to refine the modeling to analyze the shock layer for $\sigma^- < \sigma < \sigma^{\text{rear}}$, a refinement of the model which would need to describe the reopening of voids due to reverse elastic loading. In the following all results obtained in presence of micro-inertia are reported for stresses up to σ^- .

In addition, for shocks of amplitude lower than 8GPa, σ^- is not far from the shock stress level σ^{rear} and consequently σ^- can be viewed as a good approximation of the shock pressure. It is emphasized that the shock intensity is truly characterized either by the shock Lagrangian speed C or the shock pressure σ^{rear} (with $\sigma^{\text{rear}} = \sigma^-$ when micro-inertia is disregarded). This is why for all results reported here, the value of C is provided as a true signature of the shock, while σ^- stands as a close approximation of σ^{rear} .

This section focuses now on the shock structure for porous aluminium with initial porosity $f_0 = 0.03$. The porous material contains spherical voids of initial identical radius. Note that the dynamic stress is scaled by the initial size of the void, see Eq. (29). Thus the overall response of the porous material is very much dependent of the void size when high strain rate are considered. So it is worth investigating the effect of the initial void radius a_0 . Shock intensities considered in this section cover the range [1.5GPa-8GPa] (C lies between=2 495m/s and 5 217m/s, see Table 3) and a_0 is ranging from 1.5625 to 50 μm .

The analysis of the wave structure is first carried out based on the evolution of the accumulated equivalent plastic strain E_{eq}^{p} with respect to ξ for a shock intensity $\sigma^- = 5\text{GPa}$ ($C=4\,686\text{m/s}$). Fig. 9 displays results for different initial void radii. The case without micro-inertia is also superimposed. Fig. 9 clearly illustrates the transition from a sharp to a smooth evolution of the accumulated plastic strain E_{eq}^{p} as a_0 is enhanced. Besides, the case of small voids $a_0=1.5625\mu\text{m}$ is hardly distinguishable from the micro-inertia independent case in terms of E_{eq}^{p} vs ξ . This suggests that the approach where micro-inertia is disregarded (see Section 4.2) may be sufficient to describe shock structure in porous solids containing small voids when weak shock amplitudes are considered. **Large shock levels are necessary to activate micro-inertia effects when the initial void size is small.** Reminds that results shown in Fig. 9 are reported up to σ^- which is slightly lower than the equilibrium stress σ^{rear} at the rear of the shock front. Almost no evolution of E_{eq}^{p} is expected in the final stage from σ^- to σ^{rear} . This is schematically illustrated in Fig. 9 by the horizontal dashed line originated from point A attached to the curve $a_0=50\mu\text{m}$. One may also see Fig. 12 for $f_0=0.03$, $a_0=12.5\mu\text{m}$ and $\sigma^- = 3\text{GPa}$.

A different perspective of the shock structure is provided in Fig 10 (semi-log scale) where the evolution of the equivalent plastic strain rate D_{eq}^{p} versus ξ for $\sigma^- = 5\text{GPa}$ ($C=4\,686\text{m/s}$) and $f_0=0.03$ is shown. The responses of the model with two different void radii $a_0=1.5625$ and $6.25\mu\text{m}$ and the micro-inertia independent case ($a_0 \rightarrow 0$) are illustrated. We observe a very strong variation of $\max(D_{\text{eq}}^{\text{p}})$ with a_0 . When a_0 is larger, it is observed that: (i) micro-inertia is enhanced and consequently void collapse is refrained (however the material is almost fully densified near state (-)); (ii)

The distribution of D_{eq}^{p} in the shock front is broadened and the shock structure is more
 545 asymmetric.

The effect of the shock intensity is addressed in Fig.11 by considering a fixed value
 of the initial void radius $a_0=12.5\mu\text{m}$ and three shock amplitudes: $\sigma^- = 1.5, 3$ and 8GPa
 ($C=3\,007, 4\,059$ and $5\,217\text{m/s}$). Results showing the evolution of the accumulated plas-
 550 tic strain E_{eq}^{p} versus position ξ are presented in Fig.11 and are compared to predictions
 of the micro-inertia independent theory. For $\sigma^- = 1.5\text{GPa}$ ($C=3\,007\text{m/s}$), micro-inertia
 plays almost no role. An increase in the shock intensity leads to larger micro-inertia ef-
 fects evaluated by the difference between inertia dependent (dashed curves) and inertia-
 independent (solid curves) results. Further investigations on the shock width w confirm
 555 that the shock width becomes independent from the shock stress σ^- for large shock am-
 plitudes, see also Carroll et al. (1986); Nesterenko (2001).

This section ends with Fig. 12 showing the evolution of the porosity and of D_{eq}^{p} ver-
 sus ξ (Fig.12a) and the evolution of D_{eq}^{p} with respect to the accumulated plastic strain
 E_{eq}^{p} (Fig.12b). The case $f_0=0.03$, $a_0=12.5\mu\text{m}$, $\sigma^- = 3\text{GPa}$ ($C=4\,059\text{m/s}$) is considered
 here for comparison with the corresponding micro-inertia independent case addressed
 560 in Fig. 7. As previously, different stages can be defined: during stage I, the porosity is
 nearly frozen while stage II is related to the void closure process.

It should be reminded that when micro-inertia is included, the stress σ^{rear} at the
 rear of the shock may slightly differ from σ^- identified from the intersection of the
 Rayleigh line and the isothermal compression curve. Reminds also that calculations
 565 have been conducted up to σ^- . The location where σ^- is reached is shown on Fig. 12
 with a schematic illustration of further evolution (dotted lines) up to the equilibrium
 stress σ^{rear} . It appears that σ^{rear} is reached with almost no evolution of the accumu-
 lated plastic strain E_{eq}^{p} between σ^- and σ^{rear} . Moreover, the shock structure is largely
 formed and the maximum plastic strain rate is reached below σ^- such that the shock
 570 width w obtained from Eq. (56) remains representative of the shock structure even
 when micro-inertia effects are considered.

4.4. Effects of micro-inertia on shock width

In this section, we pay attention to the evolution of the shock width when the micro-inertia contribution is integrated in the modeling. We consider various initial porosities $f_0=0.03, 0.1, 0.3$, and different initial void radii still in the range $[1.5625\mu\text{m}-50\mu\text{m}]$. The stress σ^- is varying between 1 to 8GPa (see Table 3 for corresponding plastic shock speeds). Fig. 13 (semi-log scale) displays the variation of the shock width w in terms of the shock amplitude (characterized by σ^-) and synthesizes the effects of pore characteristics (initial porosity and void radius) on w .

In Fig. 13a, various initial void radii are considered for a fixed value of the initial porosity, $f_0=0.03$. As references, two limiting cases are also considered: (i) dense material (dashed line) and (ii) porous model with micro-inertia effects neglected. An important difference between dense and porous materials can be observed. For dense aluminium, the shock width decreases steadily when the shock amplitude increases while for porous aluminium, w reaches asymptotically a non-zero lower bound value for the porous viscoplasticity theory including micro-inertia effects. Note that the trend towards a stabilized (asymptotic) value is more pronounced for larger values of the initial radius a_0 . The fact that the shock width w increases with a_0 for a given value of σ^- is in agreement with the results of Fig. 9 and appears as a direct effect of micro-inertia that can be quantified by comparison with the bottom curve corresponding to the porous model without micro-inertia. In the classical approach neglecting micro-inertia, the shock width results from the balance between the steepening effect associated to the nonlinear elastic-plastic response and the smoothing effect due to nonlinear viscosity. Accounting for micro-inertia provides an additional physical factor contributing to the widening of the shock layer and allowing to reach a stabilized value of w at large shock amplitudes.

Results provided in Fig. 13a also indicate that for a given σ^- , the shock width of a porous medium may be larger than that measured in the dense medium. As an example, for $\sigma^-=5\text{GPa}$, we have $w \simeq 85\mu\text{m}$ in the dense aluminium while $w=206\mu\text{m}$ in the case of a porous medium with $f_0=0.03$ and $a_0=50\mu\text{m}$. This result can be of importance for the design of shock mitigation devices.

Results in Fig. 13b-c are relative to different values of the initial porosity and con-

firm the trends previously revealed for $f_0 = 0.03$. In addition, the shock width appears to be a decreasing function of f_0 .

605 In order to capture more precisely the link between w and the material internal structure (pore characteristics), the evolution of the shock width ratio w/a_0 has been evaluated in terms of the stress σ^- for $f_0 = 0.03, 0.1, 0.3$ and a_0 ranging from 1.5625 to $50\mu\text{m}$. Obtained results (not plotted here) show that for larger amplitude shocks, the width w is weakly depending on the stress magnitude σ^- and is scaled by a length
610 of the order of few a_0 . More specifically, for $f_0 = 0.03$, $a_0 > 6.25\mu\text{m}$ and $\sigma^- = 8\text{GPa}$, conditions under which micro-inertia effects are significant, it appears that $w \simeq 3.8a_0$. Thus, for the fixed value of the initial porosity $f_0 = 0.03$, the shock width turns out to be scaled by the material internal length a_0 (initial void size) when micro-inertia is important. The same observation holds for $f_0 = 0.1$ (resp. $f_0 = 0.3$) where under the same
615 above conditions we have $w \simeq 2.6a_0$ (resp. $w \simeq 1.6a_0$).

It is worth noting that similar relationships between microstructural length scale and shock structure can be found for granular porous materials, Carroll et al. (1986); Nesterenko (2001). In studying the effect of temperature on shock compaction of powders, Carroll et al. (1986) proposed an estimation of the shock width in the limiting case
620 of temperature and viscosity independencies. In that case, only micro-inertia plays a role in structuring the shock front. The authors established the following relationship, see Eq. (A13) in Carroll et al. (1986):

$$\left(\frac{\delta}{a_0}\right)^2 = \frac{4(2)^{1/3}\alpha_0^2}{3(\alpha_0 - 1)} \left(1 - \frac{\alpha_0 - 1}{\alpha_0 + 1}\right)^{1/3}, \quad (60)$$

where α_0 is related to the initial porosity f_0 by:

$$\alpha_0 = \frac{1}{1 - f_0}, \quad (61)$$

or similarly, in terms of f_0 , the normalized shock width δ/a_0 is expressed as:

$$\frac{\delta}{a_0} = \frac{(2)^{4/3}}{(3f_0)^{1/2} (1 - f_0)^{1/3} (2 - f_0)^{1/6}}. \quad (62)$$

625 Then, considering the set of three porosities of Fig. 13, $f_0 = 0.03, 0.1, \text{ and } 0.3$, Carroll et al. (1986) estimate provides $\delta \simeq 7.6a_0, 4.3a_0, 2.7a_0$ to be compared to $w = 3.8a_0, 2.6a_0, 1.6a_0$ obtained from our modeling. Therefore, it is clear that both normalized

shock width ratios w/a_0 and δ/a_0 decrease with larger initial porosity f_0 . Our model appears to be consistent with Carroll et al. (1986). However, the dependence of the shock width ratio to f_0 is different. This can be partly attributed to the definition of the shock width which is not identical for both approaches (see Eq. (A7) of Carroll et al. (1986) and Eq. (61) for our approach). In addition, the scaling law obtained by Carroll et al. (1986) is derived assuming that the compaction process is only micro-inertia dependent, while in our approach, even if micro-inertia is important, the shock structure results from the interplay between viscous and micro-inertia effects. For additional point of view about the link between shock structures and material internal structures, we refer to Nesterenko (2001).

4.5. Master curve for the shock width

Finally, a master curve is identified giving the shock width as a function of the shock intensity, void characteristics and matrix parameters. A dimensional analysis has been conducted from which three dimensionless quantities, π_1 , π_2 and π_3 are related by the following functional relationship, see Supplementary Material:

$$\pi_2 = \mathcal{F}\left(\pi_1, \pi_3, f_0, \frac{a_0}{b}, \underline{\pi}_{\text{matrix}}\right), \quad (63)$$

with

$$\pi_1 = \frac{\Delta\sigma}{\sigma_{a0}(1-f_0)}, \quad (64)$$

$$\pi_2 = \frac{w}{a_0 \left(\frac{1-f_0}{f_0}\right)^{1/3}} = \frac{w}{b_0(1-f_0)^{1/3}}. \quad (65)$$

$$\pi_3 = a_0 \sqrt{N_{m0}}. \quad (66)$$

$\underline{\pi}_{\text{matrix}}$ stands for a set of dimensionless parameters representative of the matrix behavior. Parameters π_1 and π_2 reflect respectively the shock intensity and the shock width. The parameter π_3 is related to the initial void radius and the initial density of mobile dislocation N_{m0} .

For the proposed analysis, various shock stress intensities $\Delta\sigma$, initial porosities and initial void radii are considered; The Burgers vector is $b=0.286 \cdot 10^{-9}\text{m}$. Two values of the initial mobile dislocation density are also considered: $N_{m0} = N_{m0}^{\text{ref}}$

650 and $N_{m0} = 4N_{m0}^{\text{ref}}$, where $N_{m0}^{\text{ref}} = 0.818 \cdot 10^{13} \text{m}^{-2}$ corresponds to the reference value adopted by Clifton (1970) and Molinari & Ravichandran (2004), see Table 1.

In Fig. 14, all results are collected in a single master curve showing the evolution of π_2 versus $\pi_1 \pi_3^\kappa$ with $\kappa = 0.278$. It appears that the dependency of π_2 in Eq. (63) with respect to f_0 and a_0/b is no more present. Therefore Eq. (63) can be simplified into:

$$\pi_2 = \mathcal{F}(\pi_1 \pi_3^\kappa, \underline{\pi}_{\text{matrix}}). \quad (67)$$

655 As illustrated in Fig. 14, the master curve is accurately described using the following relationship:

$$\pi_2(x) = k_1 + \frac{k_2}{x^{k_3}} \text{ for } x = \pi_1 \pi_3^\kappa \quad (68)$$

and $k_1=1.15$, $k_2=450$, $k_3=1.9$. Note that κ , k_1 , k_2 , k_3 and $\underline{\pi}_{\text{matrix}}$ depend on matrix properties.

For large values of $\pi_1 \pi_3^\kappa$, it is seen in Fig. 14 that π_2 is nearly constant, i.e. solely 660 dependent upon matrix properties. From the definition of π_2 given by Eq. (65), and using Eq.(68), it follows that:

$$w \simeq k_1 a_0 \left(\frac{1-f_0}{f_0} \right)^{1/3} = k_1 b_0 (1-f_0)^{1/3}. \quad (69)$$

Thus, when micro-inertia effects are important (this implies relatively large values of π_1 and π_3 , i.e. relatively large shock amplitudes and initial void radius) the shock width appears to be scaled by the initial void size a_0 (or equivalently by $2b_0$, the size 665 of the representative volume element) for a given initial porosity f_0 and a given matrix behavior.

Finally, comparing Eq. (69) with the scaling law (62) proposed by Carroll et al. (1986) shows some difference between the two models regarding the influence of the initial porosity f_0 . Note that the present scaling law (67) still contains matrix properties, while the Carroll et al. (1986) relationship (62) does not. 670

5. Conclusion

This work provides a fundamental approach of steady shock waves in porous metals. The analysis is applied to porous aluminium, but is general enough to be used for

any porous metal. Our main concern has been to uncover the relationship between the
675 material internal structure (pore characteristics) and the shock layer structure. Shock
amplitudes up to 8GPa are considered and temperature effects are disregarded. In addition,
the porosity is assumed to be relatively small (typically less than 0.3) and voids
are supposed to be isolated. Foams are not analyzed here.

Essential effects can be analyzed by assuming a simple configuration with small
680 spherical voids of same initial radius. This is sufficient to understand the role of porosity,
void size, matrix properties and micro-inertia effects on the shock structure.

We have developed a framework allowing to get the shock structure by analytical
means via the integration of a set of differential equations. A key step of the formulation
is the analytical characterization of the quasistatic compression curve which, for
685 weak shocks (up to 8GPa for porous aluminium) can be used in place of the Hugoniot
for shock analysis. For a shock of given Lagrangian speed, the shock path has been
entirely characterized based on the quasistatic compression curve and an admissibility
criterion (the chord criterion).

Of central importance in our modeling is the role played by micro-inertia effects
690 in structuring the shock front. Usual damage models, such as the classical Gurson-
Tvergaard-Needleman model of porous plasticity, do not account for the rapid acceleration
of material particles in the vicinity of collapsing (or growing) voids. As a matter
of fact, for compressive shocks the rapid collapse of micro-voids leads to local inertial
effects which affect the overall response of the porous medium as shown by Carroll &
695 Holt (1972); Dunin & Surkov (1979); Molinari & Mercier (2001). These micro-inertia
effects have been accounted for in our modeling. They are scaled by the square of
the initial void radius and therefore they are quite significant for relatively large voids.
Micro-inertia effects are very much enhanced when the shock amplitude is increased.

The rate sensitivity of the matrix flow stress also influences the shock structure. In
700 our approach, a large strain rate sensitivity of the matrix material has been taken from
the work of Molinari & Ravichandran (2004) on shocks in dense aluminium. We have
shown here that micro-inertia plays still a significant role even for materials with large
strain-rate sensitivity.

The effects of porosity, initial void radius and shock amplitude on the shock width

705 have been clarified.

The relationship between shock speed and particle velocity has been characterized and appears to reproduce closely the experimental results.

710 An important outcome is the obtention of a new scaling law relating the shock width to the initial void radius when micro-inertia effects are significant. Such situation is found by increasing the shock amplitude or the initial void size. The proposed scaling law appears consistent with the analytical scaling law of Carroll et al. (1986) obtained when only micro-inertia is structuring the shock. Our results take account for the combined effects of material parameters and micro-inertia.

715 It is believed that the fundamental findings obtained in this work can be useful to design porous metals in order to mitigate the effects of shock waves. Future developments will account for the non-uniformity of initial void size and for non-spherical void shapes, thus providing additional insight in the way of designing an optimal internal pore distribution.

References

- 720 Asay, J. R. (1975). Shock and release behavior in porous 1100 aluminum. *J. Appl. Phys.*, *46*, 197–203.
- Bakanova, A., Dudoladov, I., & Sutulov, Y. (1974). Shock compressibility of porous tungsten, molybdenum, copper, and aluminum in the low pressure domain. *J. Appl. Mech. Tech. Phys.*, *15*, 241–245.
- 725 Barthélémy, R., Jacques, N., Kerampran, S., & Vermeersch, F. (2016). Modelling of micro-inertia effects in closed-cell foams with application to acoustic and shock wave propagation. *Int. J. Solids Struct.*, *97-98*, 445–457.
- Butcher, B., Hicks, D., & Holdridge, D. (1972). *Elastic precursor decay and steady wave evolution in porous aluminium and porous polyurethane*. Technical Report SC-RR-72 0627 Sandia Labs.
- 730 Butcher, B. M., Carroll, M. M., & Holt, A. C. (1974). Shock-wave compaction of porous aluminum. *J. Appl. Phys.*, *45*, 3864–3875.
- Carroll, M. M., & Holt, A. C. (1972). Static and dynamic pore collapse relations for ductile porous materials. *J. Appl. Phys.*, *43*, 1626–1636.
- 735 Carroll, M. M., Kim, K. T., & Nesterenko, V. F. (1986). The effect of temperature on viscoplastic pore collapse. *J. Appl. Phys.*, *59*, 1962–1967.
- Clifton, R. J. (1970). On the analysis of elastic/visco-plastic waves of finite uniaxial strain. In J. J. Burke, & V. Weiss (Eds.), *Shock Waves and the Mechanical Properties of Solids* (pp. 73–116). Syracuse University Press.
- 740 Cohen, T., & Durban, D. (2015). Steady shock waves in porous plastic solids. *Int. J. Solids Struct.*, *71*, 70 – 78.
- Czarnota, C., Jacques, N., Mercier, S., & Molinari, A. (2008). Modelling of dynamic ductile fracture and application to the simulation of plate impact tests on tantalum. *J. Mech. Phys. Solids*, *56*, 1624–1650.

- 745 Czarnota, C., Mercier, S., & Molinari, A. (2006). Modelling of nucleation and void
growth in dynamic pressure loading, application to spall test on tantalum. *Int. J.*
Fract., *141*, 177–194.
- Czarnota, C., Molinari, A., & Mercier, S. (2016). Shock wave structures in porous me-
dia accounting for micro-inertia effects. 24th International Congress of Theoretical
750 and Applied Mechanics (ICTAM), Montreal, Canada, August 21-26.
- Dunin, S. Z., & Surkov, V. V. (1979). Structure of a shock wave front in a porous solid.
J. Appl. Mech. Tech. Phys., *20*, 612–618.
- Făciu, C., & Molinari, A. (2006). On the longitudinal impact of two phase transforming
bars. Elastic versus a rate-type approach. part I: The elastic case. *Int. J. Solids Struct.*,
755 *43*, 497–522.
- Gurson, A. L. (1977). Continuum theory of ductile rupture by void nucleation and
growth : Part I - yield criteria and flow rules for porous ductile media. *J. Eng. Mater.*
Technol., *99*, 2–15.
- Herrmann, W. (1969). Constitutive equation for the dynamic compaction of ductile
760 porous materials. *J. Appl. Phys.*, *40*, 2490–2499.
- Jacques, N., Czarnota, C., Mercier, S., & Molinari, A. (2010). A micromechanical
constitutive model for dynamic damage and fracture of ductile materials. *Int. J.*
Fract., *162*, 159–175.
- Johnson, J. N. (1981). Dynamic fracture and spallation in ductile solids. *J. Appl. Phys.*,
765 *52*, 2812–2825.
- Kiselev, S. P. (1995). On propagation of a shock wave in a porous material upon
collision of plates. *Combustion, Explosion and Shock Waves*, *31*, 473–477.
- Knowles, J. K. (2002). Impact-induced tensile waves in a rubberlike material. *J. Appl.*
Math., *62*, 1153–1175.
- 770 Kraus, R. G., Chapman, D. J., Proud, W. G., & Swift, D. C. (2009). Hugoniot and spall
strength measurements of porous aluminum. *J. Appl. Phys.*, *105*.

- Marsh, S. (1980). *LASL Shock Hugoniot Data*. Los Alamos Scientific Laboratory Series on Dynamic Material Properties, Vol 5. University of California Press.
- Molinari, A., & Mercier, S. (2001). Micromechanical modelling of porous materials under dynamic loading. *J. Mech. Phys. Solids*, *49*, 1497–1516. 775
- Molinari, A., & Ravichandran, G. (2004). Fundamental structure of steady plastic shock waves in metals. *J. Appl. Phys.*, *95*, 1718 – 1732.
- Morgan, D. T., Rockowitz, M., & Atkinson, A. L. (1965). *Measurement of the Grüneisen parameter and the internal energy dependence of the solid equation of state for aluminium and teflon*. Technical Report AFWL-TR-65-11 Air Force weapons Laboratory. 780
- Needleman, A., & Tvergaard, V. (1991). An analysis of dynamic, ductile crack growth in a double edge cracked specimen. *Int. J. Fract.*, *49*, 41–67.
- Needleman, A., Tvergaard, V., & Hutchinson, J. W. (1992). Void growth in plastic solids. In A. S. Argon (Ed.), *Topics in Fracture and Fatigue* (pp. 145–179). Berlin: Springer-Verlag. 785
- Nesterenko, V. F. (2001). *Dynamics of Heterogeneous Materials*. Shock Wave and High Pressure Phenomena. Springer-Verlag New York.
- Ortiz, M., & Molinari, A. (1992). Effect of strain hardening and rate sensitivity on the dynamic growth of a void in a plastic material. *J. Appl. Mech.*, *114*, 48–53. 790
- Simo, J. C., & Hughes, T. J. R. (1998). *Computational inelasticity*. Interdisciplinary applied mathematics. New York, Berlin, Heidelberg: Springer.
- Tvergaard, V. (1981). Influence of voids on shear bands instabilities under plane strain conditions. *Int. J. Fract.*, *17*, 389–407.
- Weinberg, K., & Ortiz, M. (2005). Shock wave induced damage in kidney tissue. *Comput. Mater. Sci.*, *32*, 588–593. 795

List of Figures

- 1 Schematic of the planar impact of a homogeneous equivalent medium
representative of a porous solid. The loading direction is \mathbf{e}_1 . A station-
ary shock forms beyond a certain propagation distance. 40
- 800
- 2 Quasistatic compression curves \mathcal{C}_Y for dense ($f_0 = 0$) and porous
aluminium ($f_0 = 0.0003, 0.003, 0.03, 0.1$) up to 8GPa. The com-
pression curve obtained for the small porosity $f_0 = 0.0003$ is close
to that of a dense material (corresponding to the framework of Moli-
nari & Ravichandran, 2004). Symbol ∇ is used to mark the end of
the densification process (defined when the porosity reaches 10^{-5}):
A=($\lambda_1=0.8732, \sigma=2.668$ GPa), B=(0.9463,2.214), C=(0.9770,1.737),
D=(0.9815,1.576). 41
- 805
- 3 Quasistatic compression curve \mathcal{C}_Y for porous aluminium ($f_0 = 0.1$)
and Rayleigh line defining the shock path from state (+) to state (-) for
 $\sigma^- = 1$ GPa ($C = 1727$ m/s). The Rayleigh line, of slope $-\rho_{0m}(1 - f_0)C^2$
is tangent to \mathcal{C}_Y at state (+) and intersects \mathcal{C}_Y at state (-). A straight
path connecting the elastic state (e) to state (-) leads to an ambiguous
solution. The inflection point marks the lower bound of the stress σ^-
needed to form a shock wave. 42
- 810
- 4 Comparison of theoretical $C - v^-$ curves (solid lines) against exper-
imental $C - v^{\text{rear}}$ data obtained for dense and porous aluminium al-
loys. Material parameters used in the modeling are summarized in Ta-
ble 1. Symbols refer to experimental data found in the literature, Mor-
gan et al. (1965); Bakanova et al. (1974); Asay (1975); Marsh (1980);
Kraus et al. (2009). The grey shaded area covers the range of investi-
gation considered in the present work in terms of (σ^-, f_0) 43
- 820

- 5 Shock structure when micro-inertia is disregarded showing the accu-
 825 mulated plastic strain E_{eq}^p versus position ξ for a stress amplitude σ^-
 of 3GPa. The very dilute porous material ($f_0=0.0003$) has almost
 the same response as the dense material considered by Molinari &
 Ravichandran (2004). 44
- 6 Equivalent plastic strain rate D_{eq}^p versus position ξ (semi-log scale) for
 a stress amplitude σ^- of 3GPa. Shock speeds are reported in Fig. 5. 45
- 830 7 Definition of the three stages observed in the shock structure through
 (a) the evolution of the plastic strain rate D_{eq}^p (left axis) and poros-
 ity (right axis) vs position ξ and (b) the evolution of the plastic strain
 rate D_{eq}^p vs plastic strain E_{eq}^p . During Stage I, porosity is only slightly
 835 evolving. Stage II corresponds to the part where plastic strain is mainly
 accumulated due to pore collapse. Stage III stands for the response
 of the densified medium. Calculations are for $f_0=0.03$, $\sigma^- =3\text{GPa}$
 ($C=4\,059\text{m/s}$). Micro-inertia effects are disregarded. 46
- 8 Evolution of the shock width w given by Eq. (59) in terms of the shock
 intensity σ^- for various initial porosities. Table 3 summarizes corre-
 840 sponding values of plastic shock velocities. The dense material case
 considered by Molinari & Ravichandran (2004) is retrieved by the pro-
 posed approach applied to the very dilute case ($f_0=0.0003$). Micro-
 inertia effects are disregarded. 47
- 9 Accumulated plastic strain E_{eq}^p versus position ξ for porous aluminium
 845 of initial porosity $f_0=0.03$ and various initial void radii. Calculations
 are for $\sigma^- =5\text{GPa}$ ($C=4\,686\text{m/s}$). Micro-inertia effects are enhanced
 for larger voids. Results are shown up to σ^- . The equilibrium stress,
 σ^{rear} , reached at the rear of the shock is slightly larger than σ^- due to
 micro-inertia effects. Almost no evolution of E_{eq}^p from σ^- to σ^{rear} is
 850 expected. This is schematically illustrated by a dashed line originated
 from point A (attached to the case $a_0=50\mu\text{m}$). For the case without
 micro-inertia effects, we have $\sigma^{\text{rear}} = \sigma^-$ and $E_{eq}^{p(\text{rear})} = E_{eq}^p$ 48

855	10	Equivalent plastic strain rate D_{eq}^p versus position ξ for porous aluminium of initial porosity $f_0=0.03$ and various initial void radii. Calculations are for $\sigma^- = 5\text{GPa}$ ($C=4\,686\text{m/s}$). The shock layer appears to be larger for bigger initial void radii.	49
860	11	Accumulated plastic strain E_{eq}^p versus position ξ for porous aluminium of initial porosity $f_0=0.03$ and initial void radius $a_0 = 12.5\mu\text{m}$. Calculations are for $\sigma^- = 1.5, 3, 8\text{GPa}$ ($C=3\,007, 4\,059, 5\,217\text{m/s}$).	50
865	12	Definition of different stages observed in the shock structure through (a) the evolution of the plastic strain rate D_{eq}^p (left axis) and porosity (right axis) versus position ξ and (b) the evolution of the plastic strain rate D_{eq}^p versus plastic strain E_{eq}^p . Stage I refers to the part of the shock layer where porosity is only slightly evolving. Stage II corresponds to the part where plastic strain is mainly accumulated. Calculations are for $f_0=0.03$, $a_0 = 12.5\mu\text{m}$ and $\sigma^- = 3\text{GPa}$ ($C=4\,059\text{m/s}$). For a given shock speed C , the equilibrium stress σ^{rear} at the rear of the shock front is slightly larger than σ^- due to micro-inertia effects. A schematic illustrates evolutions of E_{eq}^p and D_{eq}^p from σ^- to σ^{rear} (thin dashed lines). Almost no evolution of E_{eq}^p is expected in this final stage.	51
870	13	Shock width (semi-log scale) versus stress σ^- . Various initial porosities are considered: a) $f_0 = 0.03$, b) $f_0=0.1$, c) $f_0=0.3$. Table 3 summarizes values of shock speeds C corresponding to tested porosities and shock intensities. The initial void radius is ranging from $a_0=1.5625\mu\text{m}$ to $50\mu\text{m}$	52
875			

- 14 Evolution of the dimensionless shock width $\pi_2 = \frac{w}{b_0(1-f_0)^{1/3}}$ versus the dimensionless parameter $\pi_1\pi_3^{0.278}$ with $\pi_1 = \frac{\Delta\sigma}{\sigma_{a0}(1-f_0)}$ and $\pi_3 = a_0\sqrt{N_{m0}}$ being respectively a normalized shock amplitude and a dimensionless void radius. Symbols presented in the figure are obtained for one part with $N_{m0} = N_{m0}^{ref} = 0.818 \cdot 10^{13} \text{m}^{-2}$ and for a_0 varying in the range $[6.25-50] \mu\text{m}$, f_0 in the range $[0.03-0.3]$, σ^- in the range $[1-8] \text{GPa}$. Additional calculations are presented for $N_{m0}=4N_{m0}^{ref}$, $a_0=25 \mu\text{m}$ and f_0 in the range $[0.03-0.3]$, σ^- in the range $[1-8] \text{GPa}$. All results lie on a master curve accurately described by Eq. (68) with $k_1=1.15$, $k_2=450$, $k_3=1.9$ 53

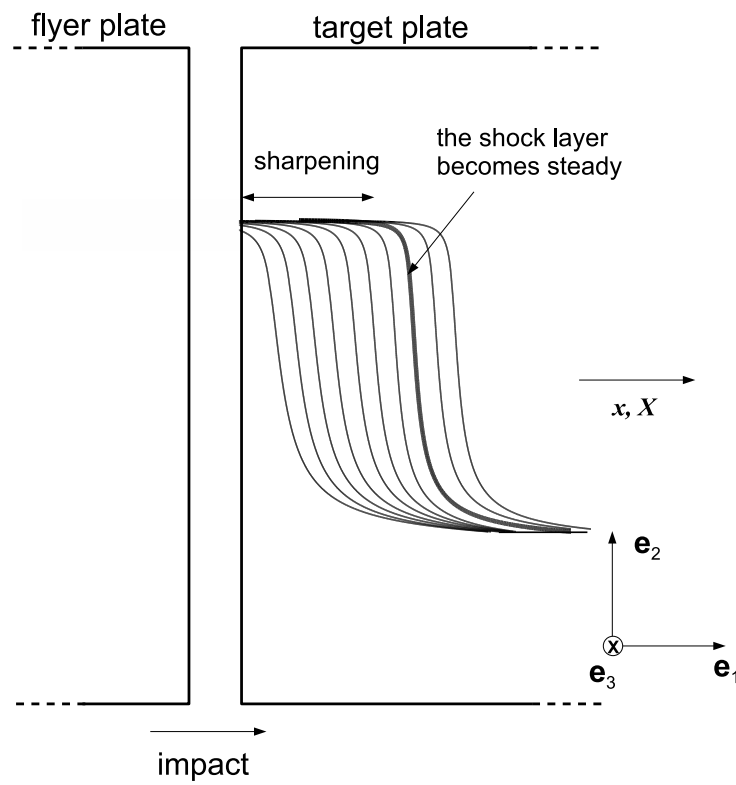


Figure 1: Schematic of the planar impact of a homogeneous equivalent medium representative of a porous solid. The loading direction is e_1 . A stationary shock forms beyond a certain propagation distance.

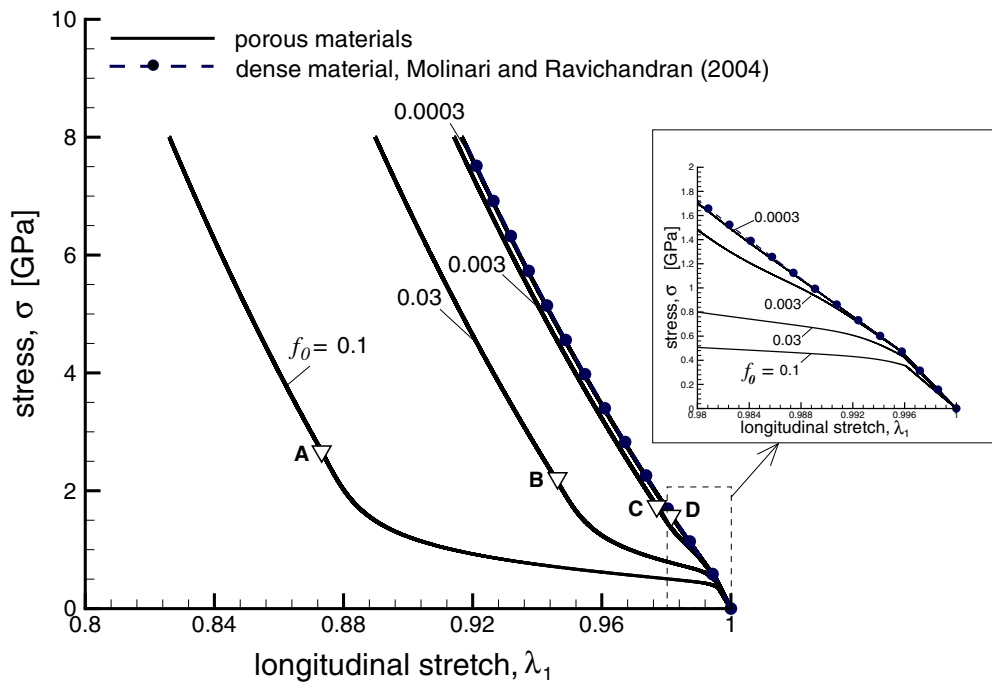


Figure 2: Quasistatic compression curves \mathcal{E}_Y for dense ($f_0 = 0$) and porous aluminium ($f_0 = 0.0003, 0.003, 0.03, 0.1$) up to 8GPa. The compression curve obtained for the small porosity $f_0 = 0.0003$ is close to that of a dense material (corresponding to the framework of Molinari & Ravichandran, 2004). Symbol ∇ is used to mark the end of the densification process (defined when the porosity reaches 10^{-5}): A=($\lambda_1=0.8732, \sigma=2.668$ GPa), B=($0.9463, 2.214$), C=($0.9770, 1.737$), D=($0.9815, 1.576$).

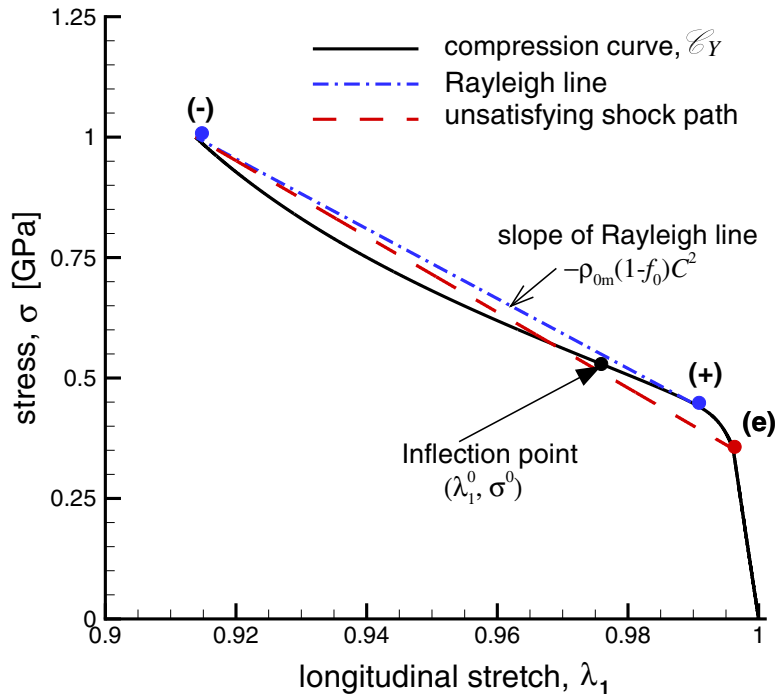


Figure 3: Quasistatic compression curve \mathcal{L}_Y for porous aluminium ($f_0 = 0.1$) and Rayleigh line defining the shock path from state (+) to state (-) for $\sigma^- = 1\text{GPa}$ ($C = 1727\text{m/s}$). The Rayleigh line, of slope $-\rho_{0m}(1-f_0)C^2$ is tangent to \mathcal{L}_Y at state (+) and intersects \mathcal{L}_Y at state (-). A straight path connecting the elastic state (e) to state (-) leads to an ambiguous solution. The inflection point marks the lower bound of the stress σ^- needed to form a shock wave.

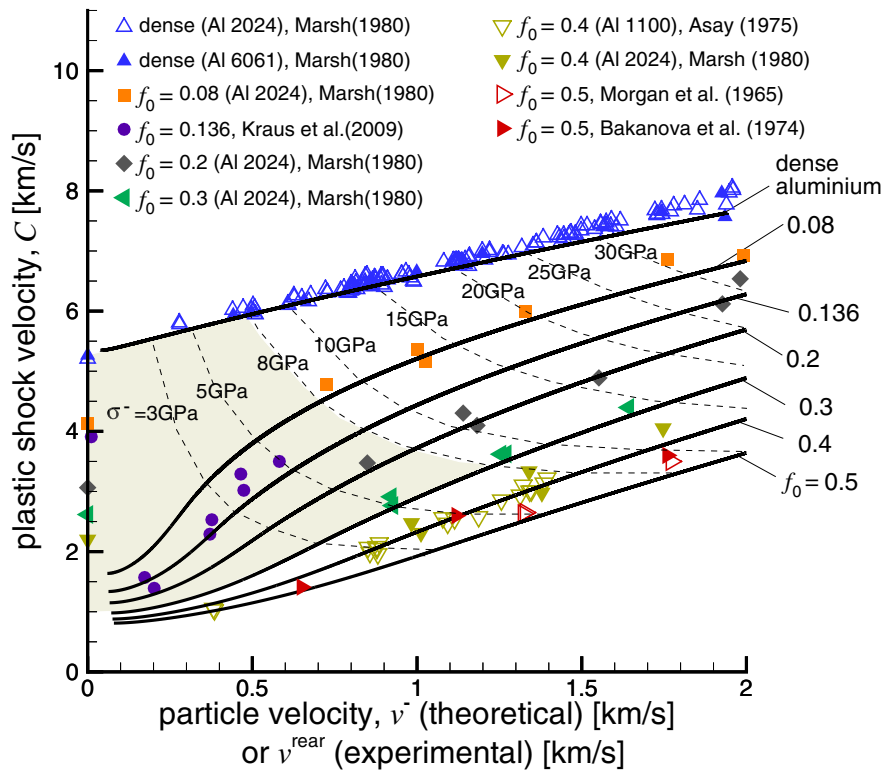


Figure 4: Comparison of theoretical $C-v^-$ curves (solid lines) against experimental $C-v^{\text{rear}}$ data obtained for dense and porous aluminium alloys. Material parameters used in the modeling are summarized in Table 1. Symbols refer to experimental data found in the literature, Morgan et al. (1965); Bakanova et al. (1974); Asay (1975); Marsh (1980); Kraus et al. (2009). The grey shaded area covers the range of investigation considered in the present work in terms of (σ^-, f_0) .

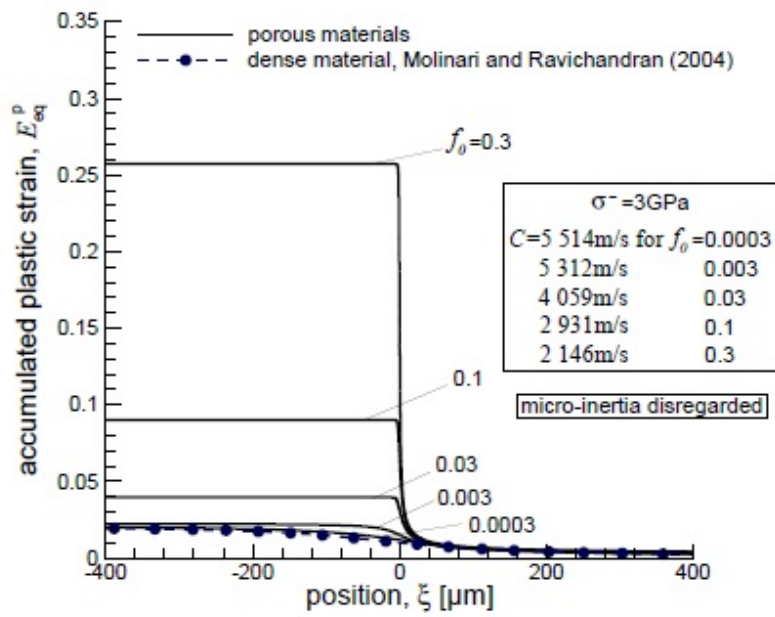


Figure 5: Shock structure when micro-inertia is disregarded showing the accumulated plastic strain E_{eq}^p versus position ξ for a stress amplitude σ^- of 3 GPa. The very dilute porous material ($f_0=0.0003$) has almost the same response as the dense material considered by Molinari & Ravichandran (2004).

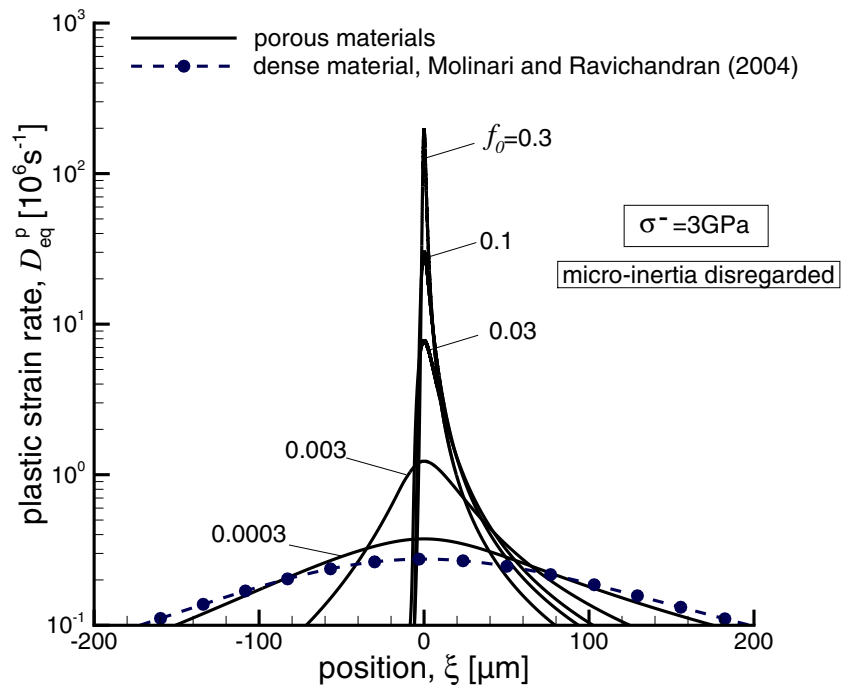


Figure 6: Equivalent plastic strain rate D_{eq}^p versus position ξ (semi-log scale) for a stress amplitude σ^- of 3GPa. Shock speeds are reported in Fig. 5.

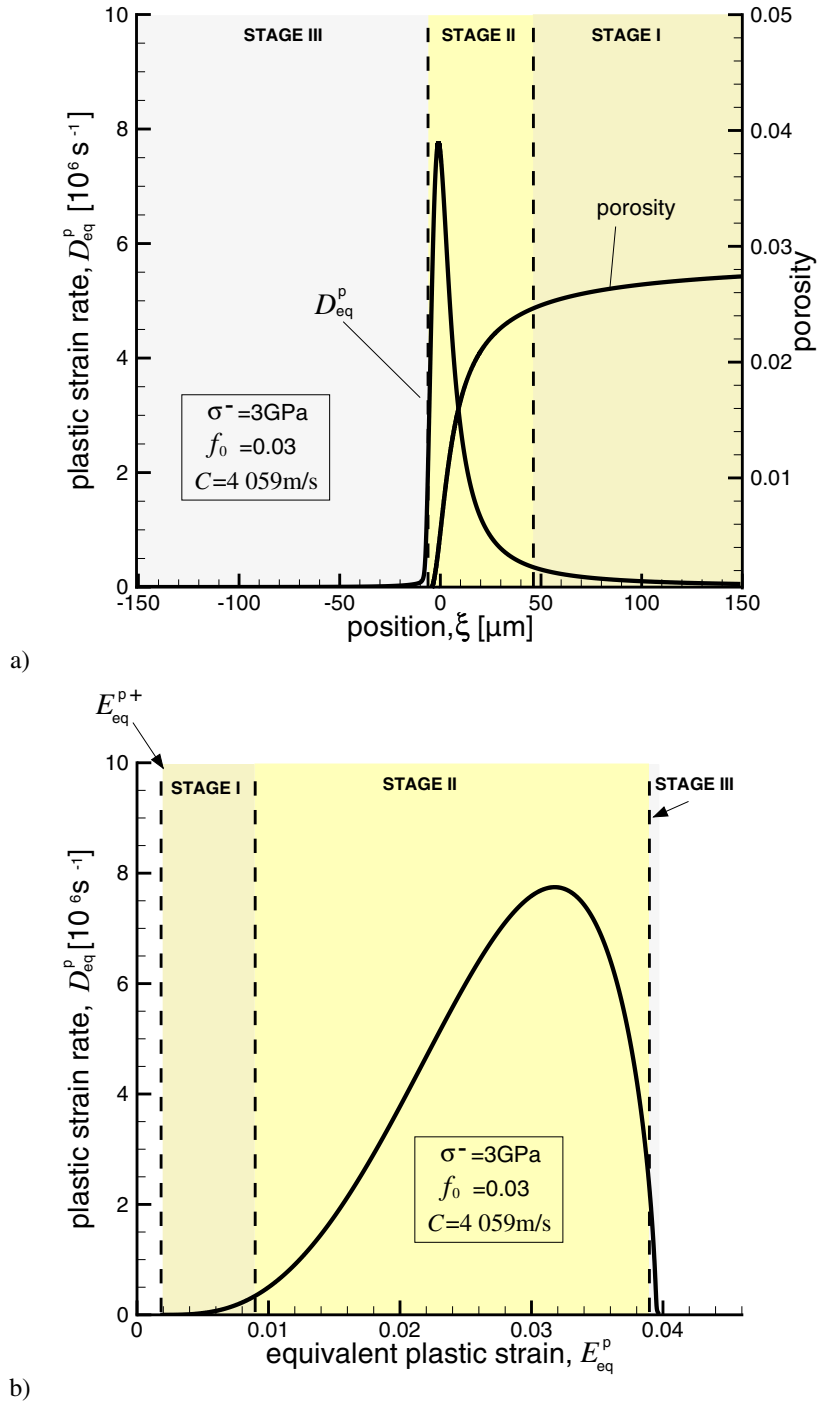


Figure 7: Definition of the three stages observed in the shock structure through (a) the evolution of the plastic strain rate D_{eq}^p (left axis) and porosity (right axis) vs position ξ and (b) the evolution of the plastic strain rate D_{eq}^p vs plastic strain E_{eq}^p . During Stage I, porosity is only slightly evolving. Stage II corresponds to the part where plastic strain is mainly accumulated due to pore collapse. Stage III stands for the response of the densified medium. Calculations are for $f_0=0.03$, $\sigma^- = 3 \text{ GPa}$ ($C=4.059 \text{ m/s}$). Micro-inertia effects are disregarded.

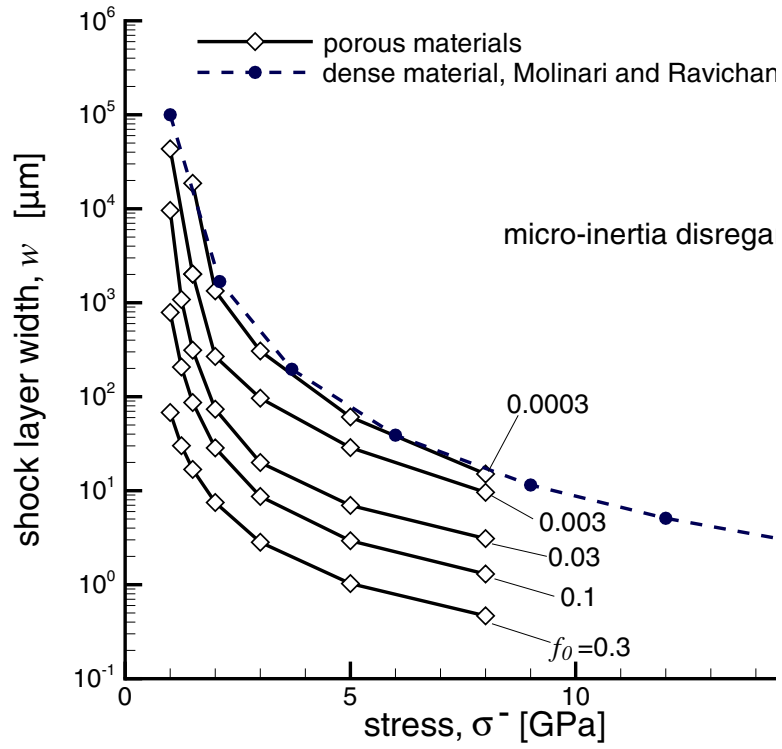


Figure 8: Evolution of the shock width w given by Eq. (59) in terms of the shock intensity σ^- for various initial porosities. Table 3 summarizes corresponding values of plastic shock velocities. The dense material case considered by Molinari & Ravichandran (2004) is retrieved by the proposed approach applied to the very dilute case ($f_0=0.0003$). Micro-inertia effects are disregarded.

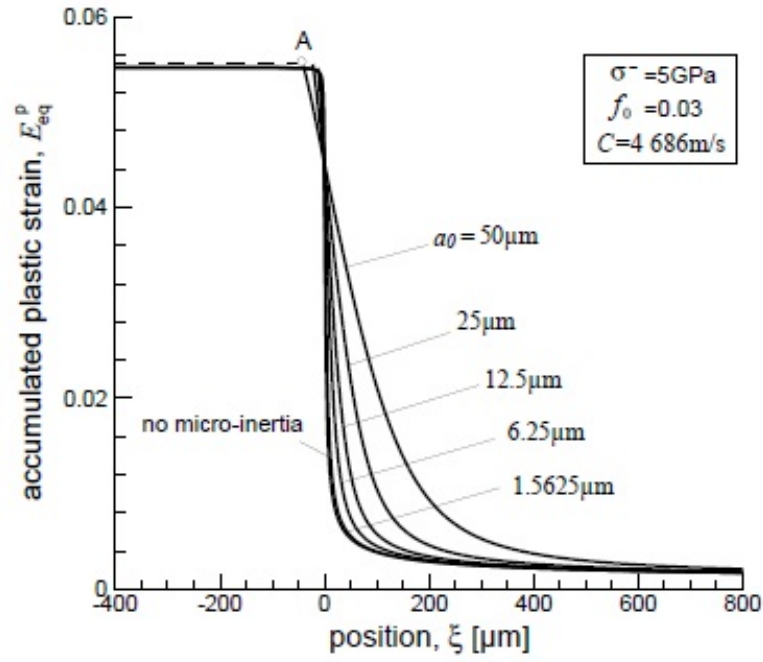


Figure 9: Accumulated plastic strain E_{eq}^p versus position ξ for porous aluminium of initial porosity $f_0=0.03$ and various initial void radii. Calculations are for $\sigma^- = 5\text{GPa}$ ($C=4686\text{m/s}$). Micro-inertia effects are enhanced for larger voids. Results are shown up to σ^- . The equilibrium stress, σ^{rear} , reached at the rear of the shock is slightly larger than σ^- due to micro-inertia effects. Almost no evolution of E_{eq}^p from σ^- to σ^{rear} is expected. This is schematically illustrated by a dashed line originated from point A (attached to the case $a_0=50\mu\text{m}$). For the case without micro-inertia effects, we have $\sigma^{\text{rear}} = \sigma^-$ and $E_{eq}^{p(\text{rear})} = E_{eq}^p$.

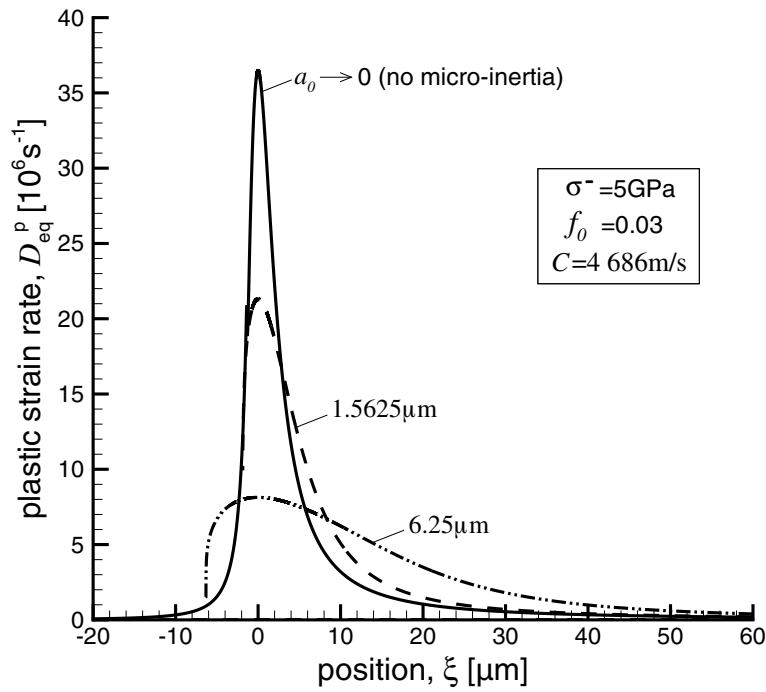


Figure 10: Equivalent plastic strain rate D_{eq}^p versus position ξ for porous aluminium of initial porosity $f_0=0.03$ and various initial void radii. Calculations are for $\sigma^- = 5\text{GPa}$ ($C=4686\text{m/s}$). The shock layer appears to be larger for bigger initial void radii.

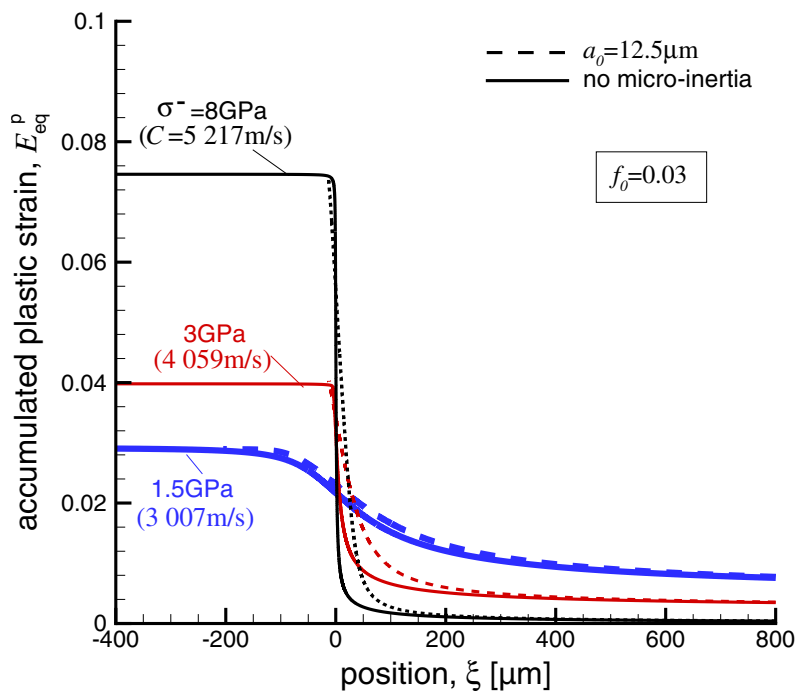


Figure 11: Accumulated plastic strain E_{eq}^P versus position ξ for porous aluminium of initial porosity $f_0=0.03$ and initial void radius $a_0 = 12.5 \mu\text{m}$. Calculations are for $\sigma^- = 1.5, 3, 8 \text{ GPa}$ ($C=3007, 4059, 5217 \text{ m/s}$).

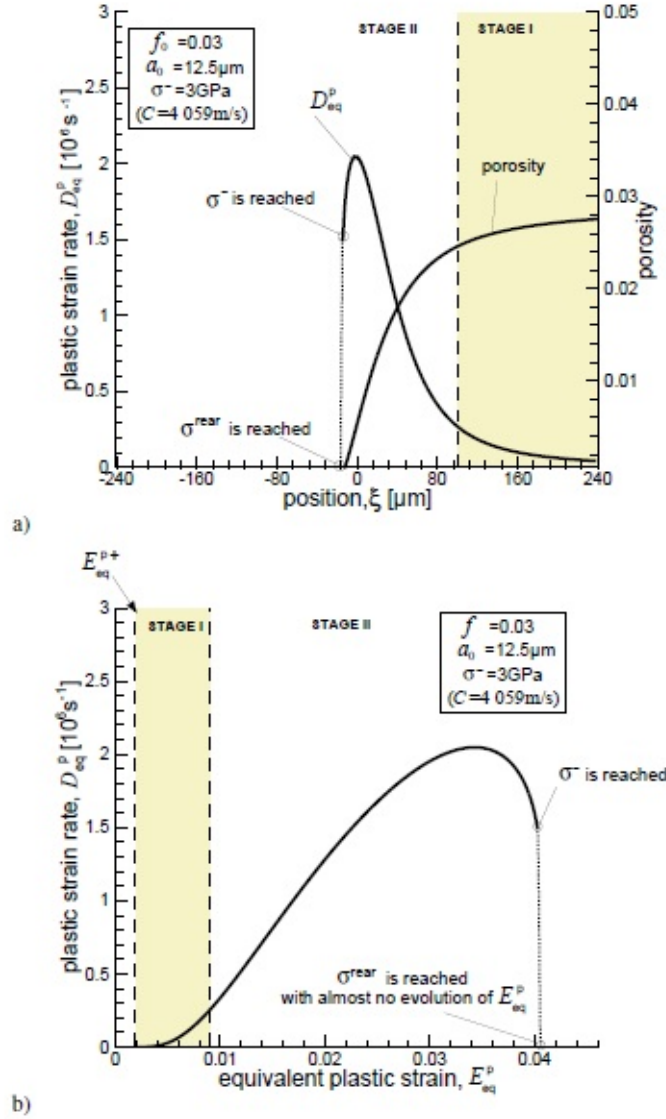


Figure 12: Definition of different stages observed in the shock structure through (a) the evolution of the plastic strain rate D_{eq}^p (left axis) and porosity (right axis) versus position ξ and (b) the evolution of the plastic strain rate D_{eq}^p versus plastic strain E_{eq}^p . Stage I refers to the part of the shock layer where porosity is only slightly evolving. Stage II corresponds to the part where plastic strain is mainly accumulated. Calculations are for $f_0=0.03$, $a_0 = 12.5 \mu\text{m}$ and $\sigma^- = 3 \text{GPa}$ ($C=4.059 \text{m/s}$). For a given shock speed C , the equilibrium stress σ^{rear} at the rear of the shock front is slightly larger than σ^- due to micro-inertia effects. A schematic illustrates evolutions of E_{eq}^p and D_{eq}^p from σ^- to σ^{rear} (thin dashed lines). Almost no evolution of E_{eq}^p is expected in this final stage.

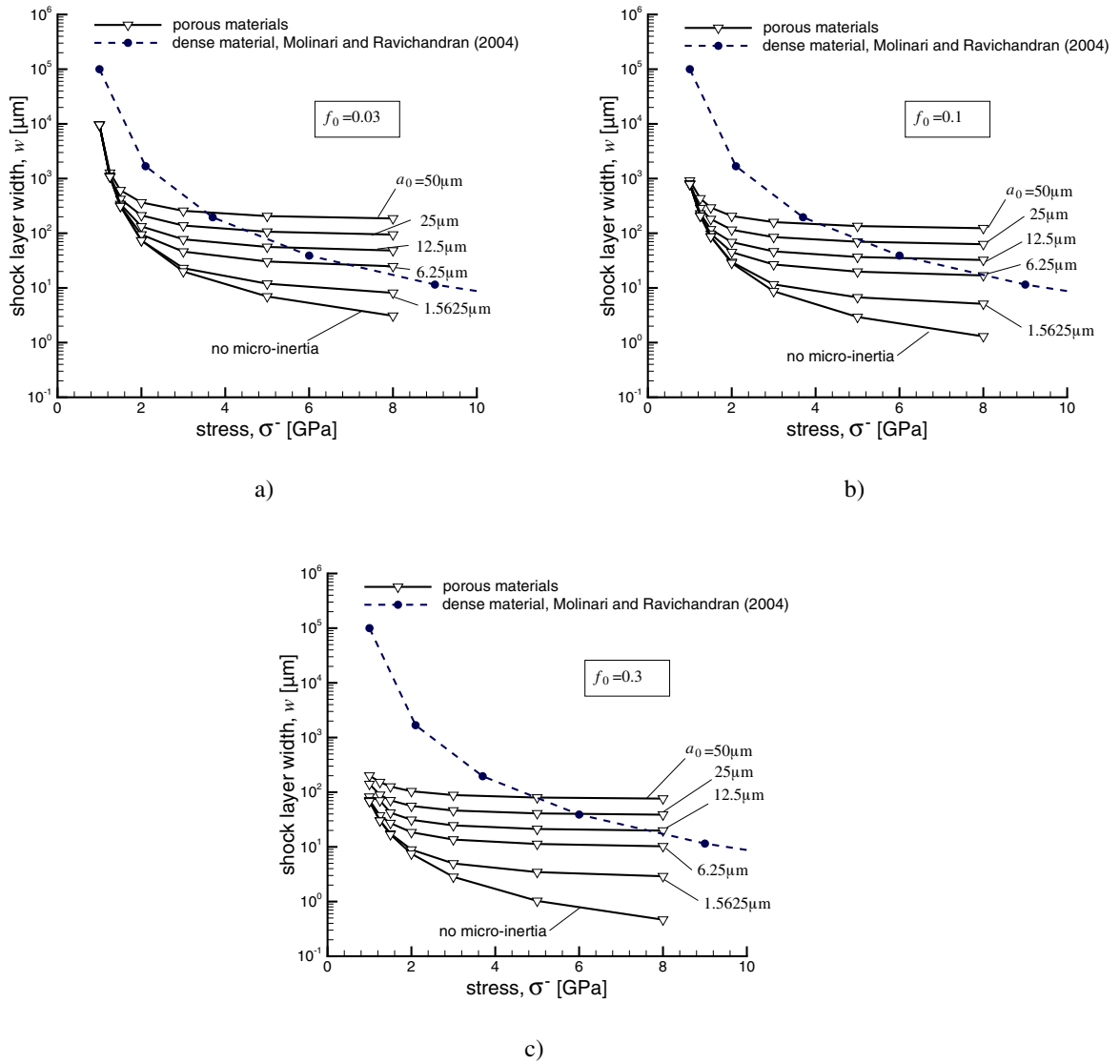


Figure 13: Shock width (semi-log scale) versus stress σ^- . Various initial porosities are considered: a) $f_0 = 0.03$, b) $f_0 = 0.1$, c) $f_0 = 0.3$. Table 3 summarizes values of shock speeds C corresponding to tested porosities and shock intensities. The initial void radius is ranging from $a_0 = 1.5625\mu\text{m}$ to $50\mu\text{m}$.

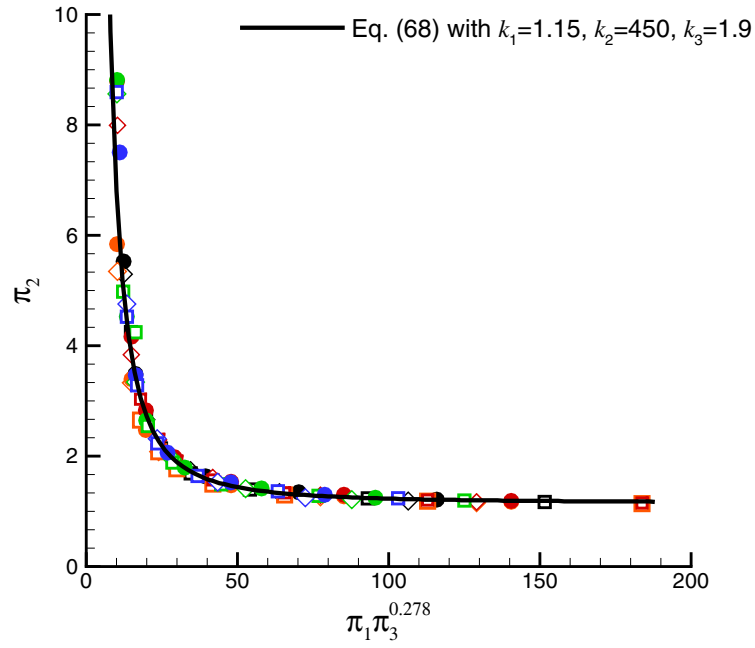


Figure 14: Evolution of the dimensionless shock width $\pi_2 = \frac{w}{b_0(1-f_0)^{1/3}}$ versus the dimensionless parameter $\pi_1\pi_3^{0.278}$ with $\pi_1 = \frac{\Delta\sigma}{\sigma_{a0}(1-f_0)}$ and $\pi_3 = a_0\sqrt{N_{m0}}$ being respectively a normalized shock amplitude and a dimensionless void radius. Symbols presented in the figure are obtained for one part with $N_{m0} = N_{m0}^{ref} = 0.818 \cdot 10^{13} \text{m}^{-2}$ and for a_0 varying in the range $[6.25-50]\mu\text{m}$, f_0 in the range $[0.03-0.3]$, σ^- in the range $[1-8]\text{GPa}$. Additional calculations are presented for $N_{m0}=4N_{m0}^{ref}$, $a_0=25\mu\text{m}$ and f_0 in the range $[0.03-0.3]$, σ^- in the range $[1-8]\text{GPa}$. All results lie on a master curve accurately described by Eq. (68) with $k_1=1.15$, $k_2=450$, $k_3=1.9$.

List of Tables

1	Material parameters for 6061-T6 aluminium at room temperature (25°C) and atmospheric pressure (from Molinari & Ravichandran, 2004, and adapted from Clifton, 1970)	55
2	Calculated stretches and stresses identifying, for various porous aluminium of initial porosity f_0 : (i) the inflection point (λ_1^0, σ^0) on the quasistatic compression curve \mathcal{C}_Y ; (ii) the elastic limit (λ_1^e, σ^e) , state (e); (iii) the state (+) characterizing the onset of the shock. Two shock levels are considered ($\sigma^- = 3$ and 8 GPa). For the dense material, there is no inflection point and σ^+ , λ_1^+ , λ_1^{p+} at state (+) coincide with corresponding quantities at state (e).	56
3	Values of the plastic shock velocity C (in ms^{-1}) calculated for various stress levels of σ^- and initial porosities f_0 considered in Figs 8 and 13.	57

Table 1: Material parameters for 6061-T6 aluminium at room temperature (25°C) and atmospheric pressure (from Molinari & Ravichandran, 2004, and adapted from Clifton, 1970)

$\rho_{0m} = 2703\text{kg/m}^3$	(mass density)
$c_L = 6368\text{m/s}$	(longitudinal wave speed)
$c_S = 3197\text{m/s}$	(shear wave speed)
First and second order thermoelastic constants	
$a_2 = c_L^2/2 = 20.28 \times 10^6 (\text{m/s})^2$; $a_3 = -2c_S^2 = -20.44 \times 10^6 (\text{m/s})^2$; $a_4 = -66.4 \times 10^6 (\text{m/s})^2$	
$a_5 = 157.5 \times 10^6 (\text{m/s})^2$; $a_6 = -142.8 \times 10^6 (\text{m/s})^2$	
Rate independent plasticity characteristics, see Eq.(27)	
$\sigma_{a0} = 240\text{MPa}$	(stress at zero plastic strain)
$\gamma_0 = 0.52$	(reference strain)
$n = 1.55$	(hardening parameter)
Rate dependent properties, see Eqs.(23) to (25)	
$M = 1.78$	(inverse of the strain rate sensitivity)
$c_1 = 0.168\text{m/s}$	
$T_1^* = 1.6\text{MPa}$	
$b = 0.286 \times 10^{-9}\text{m}$	(magnitude of the Burgers vector)
$N_{m0} = 0.818 \times 10^{13}\text{m}^{-2}$	(initial mobile dislocation density)
$N_{t0} = 0.818 \times 10^{13}\text{m}^{-2}$	(initial total dislocation density)
$\alpha_b = 3.5 \times 10^5\text{m}^{-1}$	(breeding coefficient)
$\alpha_t = 0\text{m}$	(trapping coefficient)

Table 2: Calculated stretches and stresses identifying, for various porous aluminium of initial porosity f_0 : (i) the inflection point (λ_1^0, σ^0) on the quasistatic compression curve \mathcal{C}_Y ; (ii) the elastic limit (λ_1^e, σ^e), state (e); (iii) the state (+) characterizing the onset of the shock. Two shock levels are considered ($\sigma^- = 3$ and 8GPa). For the dense material, there is no inflection point and $\sigma^+, \lambda_1^+, \lambda_1^{p+}$ at state (+) coincide with corresponding quantities at state (e).

f_0	0	0.0003	0.003	0.03	0.1	0.3
λ_1^e	0.99578 [†]	0.99578	0.99579	0.99593	0.99610	0.99595
σ^e [GPa]	0.473 [†]	0.472	0.468	0.428	0.353	0.222
λ_1^0	no inflection	0.99415	0.98647	0.98557	0.97591	0.95095
σ^0 [GPa]	no inflection	0.598	1.076	0.720	0.529	0.323
Values of $\lambda_1^+, \lambda_1^{p+}$ and σ^+ for $\sigma^- = 3$ GPa						
λ_1^+	0.99578	0.99576	0.99559	0.99367	0.99461	0.99578
λ_1^{p+}	1	1	0.99988	0.99810	0.99855	0.99984
f^+	0	0.0003	0.003	0.02961	0.09943	0.29992
σ^+ [GPa]	0.473	0.473	0.483	0.547	0.394	0.223
Values of $\lambda_1^+, \lambda_1^{p+}$ and σ^+ for $\sigma^- = 8$ GPa						
λ_1^+	0.99578	0.99578	0.99579	0.99593	0.99609	0.99594
λ_1^{p+}	1	1	1	1	0.99999	0.99999
σ^+ [GPa]	0.473	0.472	0.468	0.428	0.353	0.222
f^+	0	0.0003	0.003	0.03	0.1	0.3

[†] Molinari & Ravichandran (2004)

Table 3: Values of the plastic shock velocity C (in ms^{-1}) calculated for various stress levels of σ^- and initial porosities f_0 considered in Figs 8 and 13.

σ^- [GPa]	f_0	0	0.0003	0.003	0.03	0.1	0.3
1		5 363	no shock ¹	no shock	$C=2\,495\text{ms}^{-1}$	1 727	1 273
1.25		5 382	5 299	4 483	2 747	1 898	1 398
1.5		5 404	5 341	4 747	3 007	2 071	1 520
2		5 448	5 410	5 075	3 471	2 400	1 749
3		5 538	5 514	5 312	4 059	2 931	2 146
5		5 710	5 696	5 573	4 686	3 627	2 752
8		5 945	5 936	5 856	5 217	4 299	3 413

¹ No shock can be formed when $f_0=0.0003$, $\sigma^-=1\text{GPa}$, due to a second inflection point observed near σ^- on the quasistatic compression curve \mathcal{C}_Y .

Appendix A. Totally densified material

Equations governing the behavior of a totally densified material are provided in this appendix. Consider a porous material of initial porosity $f_0 \neq 0$. Once the material is
 905 totally densified ($f = 0$), micro-inertia contribution is no more involved in the modeling. The volumetric plastic strain rate vanishes ($D_m^p = 0$) since the matrix is assumed plastically incompressible. Subsequently, according to Eq. (15), the equivalent strain rate D_{eq}^p is given by:

$$D_{eq}^p = -\frac{\dot{\lambda}_1^p}{\lambda_1^p}. \quad (\text{A.1})$$

The nonlinear elastic response (18) becomes :

$$T_1 = \frac{\rho_{0m}(1-f_0)}{\lambda_1^p} F_1(\varepsilon_1^e, \varepsilon_2^e), \quad (\text{A.2a})$$

$$T_2 = \rho_{0m} [(1-f_0)\lambda_1^p]^{1/2} F_2(\varepsilon_1^e, \varepsilon_2^e), \quad (\text{A.2b})$$

where functions $F_i(\varepsilon_1^e, \varepsilon_2^e)$ are given by Eq. (20). The elastic strains are given in that case by:

$$\varepsilon_1^e = \lambda_1^e - 1 = \frac{\lambda_1}{\lambda_1^p} - 1, \quad (\text{A.3a})$$

$$\varepsilon_2^e = \lambda_2^e - 1 = \left(\frac{\lambda_1^p}{1-f_0} \right)^{1/2} - 1. \quad (\text{A.3b})$$

910 For dense materials, the viscoplastic flow surface (34) reduces to the von Mises flow theory:

$$\Omega_{vm} = \left(\frac{\Sigma_{eq}}{\bar{\sigma}} \right)^2 - 1 = 0 \quad (\text{A.4})$$

leading to $\Sigma_{eq} = \bar{\sigma}$, where $\bar{\sigma}$ is the equivalent flow stress of the matrix. As a consequence, the equivalent viscoplastic strain rate is:

$$D_{eq}^p = \dot{\kappa} \frac{\partial \Omega_{vm}}{\partial \Sigma_{eq}} = \frac{2\dot{\kappa}}{\Sigma_{eq}}. \quad (\text{A.5})$$

The rate of plastic work, Eq. (35), reads:

$$\Sigma : \mathbf{D}^p = \Sigma_{eq} D_{eq}^p = \bar{\sigma} \dot{\varepsilon}_{eq}^p, \quad (\text{A.6})$$

915 which induces $D_{eq}^p = \dot{\varepsilon}_{eq}^p$. The plastic multiplier is deduced: $\dot{\kappa} = D_{eq}^p \Sigma_{eq} / 2$. The plastic behavior of the matrix is still described by Eqs (22) to (27).

Combining Eqs (A.1) and (36) with $D_{\text{eq}}^{\text{p}} = \dot{\epsilon}_{\text{eq}}^{\text{p}}$, one has:

$$\frac{\dot{\lambda}_1^{\text{p}}}{\lambda_1^{\text{p}}} = -\frac{2\Phi}{3}. \quad (\text{A.7})$$

Introducing γ^{p} given by Eq. (22) and noting that $\dot{\lambda}_1^{\text{p}} < 0$ in compression, it is found that:

$$\gamma^{\text{p}} = \gamma_f^{\text{p}} - \frac{3}{2} \ln \left(\frac{\lambda_1^{\text{p}}}{\lambda_{1f}^{\text{p}}} \right), \quad (\text{A.8})$$

920 where γ_f^{p} and λ_{1f}^{p} are the accumulated plastic shear strain and plastic stretch up to the state of complete pore closure.

The particular case of initially dense material is obtained here by setting $f_0 = 0$, $\gamma_f^{\text{p}} = 0$ and $\lambda_{1f}^{\text{p}} = 1$, such that the modeling of Molinari & Ravichandran (2004) is retrieved. When $f_0 \neq 0$, the response is different because of the strain history
925 developed during the pore collapse stage.

Note that in the modeling initially developed by Molinari & Ravichandran (2004), the yield condition relates to the yield stress in pure shear and the Cauchy maximum shear stress $\tau = -\Sigma_{\text{eq}}/2$. The present approach and that of Molinari & Ravichandran (2004) coincide by setting $\sigma_{a0} = 2\tau_{a0}$ in Eq. (27) (with τ_{a0} taken from Molinari &
930 Ravichandran, 2004), and considering that $\bar{\sigma} = -2\tau$ in Eq. (26).